

InDeed: Interpretable image deep decomposition with guaranteed generalizability

Sihan Wang, Shangqi Gao, Fuping Wu, Xiahai Zhuang*

Abstract—Image decomposition aims to analyze an image into elementary components, which is essential for numerous downstream tasks and also by nature provides certain interpretability to the analysis. Deep learning can be powerful for such tasks, but surprisingly their combination with a focus on interpretability and generalizability is rarely explored. In this work, we introduce a novel framework for interpretable deep image decomposition, combining hierarchical Bayesian modeling and deep learning to create an architecture-modularized and model-generalizable deep neural network (DNN). The proposed framework includes three steps: (1) hierarchical Bayesian modeling of image decomposition, (2) transforming the inference problem into optimization tasks, and (3) deep inference via a modularized Bayesian DNN. We further establish a theoretical connection between the loss function and the generalization error bound, which inspires a new test-time adaptation approach for out-of-distribution scenarios. We instantiated the application using two downstream tasks, *i.e.*, image denoising and unsupervised anomaly detection, and the results demonstrated improved generalizability as well as interpretability of our methods. The source code will be released upon the acceptance of this paper.

Index Terms—Image decomposition, variational inference, deep learning, generalizability, image denoising, unsupervised anomaly detection, interpretability



1 INTRODUCTION

IMAGE decomposition has shown great potential in subsequent tasks, such as image denoising and anomaly detection [1]–[4]. There are two commonly seen scenarios of applications. One is to extract representative contents, such as the smoothness components, for which the total variation (TV) technique has been widely used [5]. The other is to decompose images into compositional parts. Typical methods include the robust principal component analysis [6] and multi-resolution analysis [7]. The former models data matrices as the superposition of low-rank and sparse components, which can be solved via convex optimization; the latter typically transforms an image into components at different scales or resolutions. These methods could be time-consuming when applied to downstream tasks [2], [8].

Deep learning-based approaches have shown substantial promise, but recent efforts on image decomposition mainly focus on directly simulating traditional algorithms or heuristic decomposition approaches. The simulation methods approximate the mapping of a specific method, such as the neighborhood filter [9] and TV-related frameworks [10], [11]; the typical heuristic approaches include the idea of “internal patch recurrence” [12] and the extraction of homogeneous components [3], [13], [14]. To date, most deep learning-based algorithms adopt black-box architectures, which present two significant challenges: (i) limited interpretability due to lack of transparency in the image decomposition process; and (ii) poor generalizability

in out-of-distribution (OOD) scenarios. Recently, active interpretability, also known as *ad-hoc* interpretability, has gained ample attention, although it remains underrepresented among the literature [15]. Unlike *post-hoc* methods, which try to explain the black box, the *ad-hoc* ones actively design the architecture and/or training process to achieve *model-self* interpretability [15], [16]. A notable work is the deep unrolling, which creates links between specific iterative algorithms and deep learning [17], and is applicable to various tasks, including image super-resolution, blind image deblurring, and image denoising [17]–[19]. For image decomposition, several methods have been developed with architectures guided by filters [20] or variational priors [2], [21]. Although these methods have demonstrated generalizability in downstream tasks [17], [19], [21], the exploration in image decomposition remains limited.

Herein, we propose a new framework for interpretable deep image decomposition and instantiate its application with two tasks, *i.e.*, image denoising, and unsupervised anomaly detection. The proposed framework combines Bayesian inference and deep learning, and it consists of three steps, *i.e.*, (1) hierarchical Bayesian modeling, (2) transforming the inference into optimizations, and (3) deep inference. In the first step, we decompose an image into statistically or semantically meaningful components, such as low-rank, sparsity, and noise, and then further decompose these components into sub-components to accommodate more priors. Such decomposition is applied recursively via a probabilistic graphic model (PGM) with a hierarchical structure, also known as Hierarchical Bayesian Modeling (HBM). In the second step, we adopt the variational inference for the HBM, namely approximating the posteriors. This step results in two optimization sub-problems, of which one has a closed-form solution. In the third step, We design an architecture-modularized deep neural network (DNN)

- S. Wang and X. Zhuang are with the School of Data Science, Fudan University, Shanghai, China.
- S. Gao is with the Department of Oncology, University of Cambridge.
- F. Wu is with the Nuffield Department of Population Health, Oxford University.
- X. Zhuang* is the corresponding author. E-mail: zXH@fudan.edu.cn

to infer the posteriors, with its architecture based on the HBM in the first step and its training strategy guided by the variational inference in the second step. *This framework ensures improved interpretability and generalizability for the deep image decomposition models.*

The **interpretability** originates from the integration of HBM and deep learning, resulting in *ad-hoc* design for both the architecture and training strategy. The architecture is modularized according to the HBM, incorporating explicit computations and non-linear mappings to infer the posteriors of corresponding variables, providing interpretable intermediate outputs and a self-explanatory architecture. Furthermore, the deep framework mimics the optimization process, and the DNN training strategy is guided by two sub-problems derived from variational inference, resulting in a meaningful loss function.

The **generalizability** benefits from Bayesian learning and hierarchical modeling. Firstly, we utilize PAC-Bayesian Theory to provide a generalization error bound [22], [23], demonstrating that minimization of the loss function aligns with minimization of this error bound. Secondly, the hierarchical structure enhances generalizability by fostering the interdependence between variables [21], which facilitates a sample-specific prior for meaningful components. Furthermore, inspired by the error bound and the modularized architecture, we then propose a test-time adaptation algorithm for OOD scenarios.

Our contributions are summarized as follows:

- We propose a new framework to establish an interpretable deep image decomposition. This framework consists of three steps to integrate hierarchical Bayesian modeling and deep learning.
- We establish the theoretical connection between the objective for model training and the generalization error upper bound. Inspired by this connection, we further propose a test-time adaptation algorithm, which allows for rapid adjustment of the model for OOD scenarios.
- We develop a modularized architecture driven by decomposition modeling to capture targeted components. For the low-rank component in image decomposition, we propose a tailored network that enables learning-based low-rank estimation while allowing for flexible rank adaptation.
- We validate the deep image decomposition framework on two downstream tasks, *i.e.*, image denoising and unsupervised anomaly detection, and the proposed methods demonstrate superior performance.

2 RELATED WORKS

2.1 Image decomposition

Image decomposition has gained significant attention, driven by the assumption that underlying data often lies in a low-dimensional subspace [6], [8], [24], [25], offering strong potential in image analysis. Among these techniques, low-rank estimation is attractive with theoretical advances [6], [26], leading to potential modeling options for numerous applications, such as image denoising, anomaly detection, and face recognition.

PCA demonstrates that the low-rank components of matrices are its principal components [8], [25], but it often fails with corrupted images. Robust Principal Component Analysis (Robust PCA) [6] shows that a corrupted data matrix can be decomposed into a low-rank and a sparse component, with theoretical guarantees. Although it can recover the low-rank component exactly, solving RPCA is NP-hard. Considerable efforts have been made to address this, including the accelerated proximal gradient method by Lin *et al.* [27] and the augmented Lagrange multiplier method [28], which is considered the state-of-the-art for RPCA. However, tuning parameters for optimal performance remains a challenge. Bayesian methods have been introduced to address this, using techniques like Gibbs sampling [29] and variational inference [8] for posterior inference. Despite these advances, the high computational complexity of these methods limits their real-time application.

Recently, deep learning-based image decomposition methods have emerged. Due to the black-box nature of deep neural networks, developing interpretable deep decomposition models remains challenging. Ulyanov *et al.* [1] introduced the "Deep Image Prior" to capture low-level statistics from a single image, and Gandelsman *et al.* [3] used multiple generator models to decompose images into basic components. More interpretable methods have since been explored, such as RONet for rank-one decomposition [30], and BayeSeg proposed the appearance-structure decomposition for medical image segmentation [21]. However, research on interpretability and generalizability in terms of deep image decomposition remains limited, warranting further exploration.

2.2 Image denoising

Image-denoising approaches can be broadly classified into two categories: traditional model-based methods [31]–[33] and deep learning-based methods [34]–[37]. Traditional methods explicitly model the image prior, such as total variation [38] and low-rank estimation [39], and are generally agnostic to the type of noise [40]. While these methods demonstrate good generalizability, they often fall short in accurately reconstructing image content. Deep learning-based algorithms have shown remarkable promise. Various techniques have been introduced to enhance the capabilities, including residual networks [35], [37], encoder-decoder structures [36], and self-similarity approaches [34].

Recently, methods with active interpretability have been proposed for this task. For example, Huy Vu *et al.* proposed a deep unrolling network, which integrates the classical graph total variation [41]. Liu *et al.* proposed an interpretable model for both image generation and restoration (*e.g.* denoising) by decoupling the conventional single denoising diffusion process into residual diffusion and noise diffusion [42]. These models are typically trained on Gaussian noise in controlled laboratory settings, which can limit their generalizability. To address this, previous research has focused on generating more realistic noise for training or exposing the networks to a broader spectrum of noise types. Chen *et al.* proposed a self-learning strategy that enhances the generalizability by reconstructing masked random pixels of the input image [43]. Despite these advancements, the

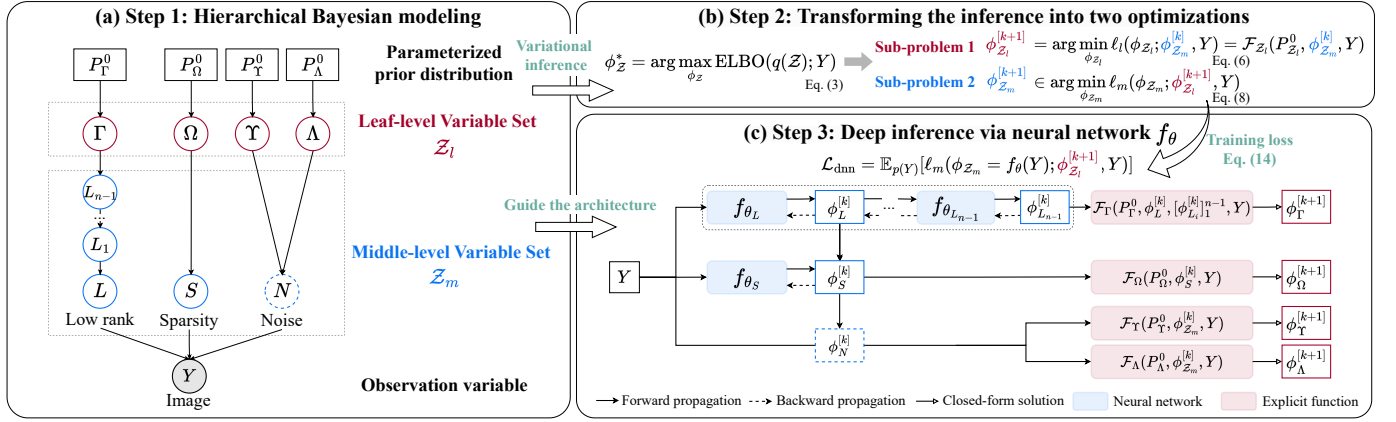


Fig. 1: The proposed three-step framework for establishing architecture-modularized and interpretable DNN. Each subfigure illustrates the corresponding step, with Step 3 being developed under the guidance of Steps 1 and 2. Note that the variable N in (a) is marked with a dotted circle, signifying that no inference is required. Function $\mathcal{F}_X(\cdot)$ in (b) and (c) denotes closed-form solution(s) w.r.t. variable(s) X .

combination of interpretability and generalizability remains under-explored.

2.3 Unsupervised anomaly detection

Recent research on unsupervised anomaly detection (UAD) can be classified into two settings, namely, class-specific UAD [44], [44]–[46] and unified UAD (UUAD) [47]. The former targets the detection of a specific class of objects with a single model [44]–[46], and the latter tackles a more challenging but vital issue, that is to develop a unified model for the detection of various classes [47]. Class-specific UAD methods mainly focus on the modeling of normality and identifying the outliers as anomalies. Mainstream approaches could be classified into three types, *i.e.*, reconstruction-based [44], [48]–[53], self-learning-based [54]–[57], and feature extraction-based methods [58]–[60]. Despite different techniques, these methods attempt to learn a better representation of the in-distribution samples. Recently, UUAD has attracted increasing attention, albeit to a limited number of publications [47]. UniAD [47] follows the idea of class-specific UAD and aims to design a powerful architecture to capture various in-distribution representations for outliers detection. However, despite the recent promising performances, further study in terms of interpretable and generalizable class-free anomaly detection is required.

3 METHODOLOGY

In this work, we propose a new framework to develop an architecture-modularized and interpretable deep neural network for image decomposition. This framework consists of three steps, and in the following, we first summarize the three steps in Section 3.1. Then, we elaborate on each step in sections of 3.2, 3.3 and 3.4, respectively. In Section 3.5, we analyze the generalization error bound and propose an algorithm for test-time adaptation in out-of-distribution (OOD) scenarios. Finally, we instantiate two downstream applications, *i.e.*, image denoising and unsupervised anomaly detection in Section 3.6.

TABLE 1: Summary of mathematical notions and corresponding notations.

Notation	Notion
Lowercase letter	Scalar (<i>e.g.</i> , a)
Bold lowercase letter	Vector (<i>e.g.</i> , \mathbf{a})
Capital letter	Matrix (<i>e.g.</i> , \mathbf{A})
$\ \cdot\ _2$; $\ \cdot\ _F$; $\langle \cdot, \cdot \rangle_F$	ℓ_2 norm; Frobenius norm; Frobenius inner product
$Y \in \mathbb{R}^{h \times w}$	Image
$U \in \mathbb{R}^{h \times w}$	Target (Ground-Truth)
$L \in \mathbb{R}^{h \times w}$	Low rank variable ($L = AB^T$)
$A \in \mathbb{R}^{h \times r^0}$	Left factor of low rank component
$B^T \in \mathbb{R}^{r^0 \times w}$	Right factor of low rank component
$S \in \mathbb{R}^{h \times w}$	Sparsity variable
$N \in \mathbb{R}^{h \times w}$	Noise variable
$\ell_X^{(i)}$; $\mathcal{L}(\cdot)/\hat{\mathcal{L}}(\cdot)$	Loss term of X for sample i ; expected/ empirical loss
$q(\cdot)$, $q_\phi(\cdot)$	Variational distribution, parameterized by ϕ
ϕ_Z	Variational parameters for variable set Z
$\phi_Z^{[k]}$	Variational parameters for Z at the k -th iteration
$\mu_X, \sigma_X / \alpha_Y, \beta_Y$	Gaussian/ Gamma distribution parameters of variable X / Y
$f_\theta(\cdot)$; $f_{\theta_X}(\cdot)$	DNN parameterized by θ ; DNN w.r.t. X with θ_X
$\mathcal{F}_Z(\cdot)$	Explicit functions w.r.t. Z
\mathcal{D} ; $ \mathcal{D} $	Dataset, the size of a dataset
$h \times w$; k	Image size; iteration index
x^0 (<i>e.g.</i> , r^0)	Hyper-parameters (<i>e.g.</i> , the maximal rank)

3.1 The three-step framework: A summary

Fig. 1 illustrates the three-step framework. In the first step, we employ hierarchical Bayesian modeling (HBM) to describe the procedure of image decomposition and incorporation of prior knowledge. This modeling results in a structured graph, which is also referred to as the probabilistic graphical model (PGM). In the second step, we use variational inference to approximate the posteriors from the HBM. This step leads to two optimization problems, of which one has closed-form solutions. In the third step, we solve the other optimization problem using a modularized Bayesian deep neural network (denoted as f_θ), thus this step is referred to as *deep inference*. These three steps are described in the sections of 3.1.1, 3.1.2 and 3.1.3, respectively.

Note that the architecture of this neural network (f_θ) follows the structure of the PGM in the first step, and its training is guided by the optimization problems in the second step. Hence, we refer to f_θ as being architecture-modularized and interpretable. In Section 3.1.4, we analyze the interpretability, modularity, and generalizability of this neural network.

3.1.1 Modeling of image decomposition

In the following, we describe the methodological formulations. For convenience, we list in Table 1 the essential mathematical symbols used in this paper.

Following the conventional decomposition rule [6], an image observation $Y = [y_{ij}]_{h \times w}$ can be modeled as a superposition of three components, *i.e.*, the low rank, the sparsity, and the noise, which are denoted respectively by three variables, $L = [l_{ij}]_{h \times w}$, $S = [s_{ij}]_{h \times w}$, and $N = [n_{ij}]_{h \times w}$. Therefore, we have $Y = L + S + N$, and the likelihood function can be written as follows,

$$p(Y|L, S) = \mathcal{N}(Y - (L + S) | \Upsilon, \Lambda^{-1}), \quad (1)$$

assuming the noise follows a normal distribution \mathcal{N} with element-wise mean Υ and inverse variance (precision) Λ .

As the PGM in Fig. 1 (a) shows, the observed variable Y is decomposed into three non-observation components, *i.e.*, N , S and L , each represented with varying levels of hierarchical structure. **For** N , no middle-level variable is involved; we directly model the leaf-level variables, *i.e.*, Υ and Λ , following the likelihood in Eq. (1), with their prior distributions P_{Υ}^0 and P_{Λ}^0 . Consequently, N is represented with a dotted circle to indicate that no inference is required. **For** S , we do not further decompose it, but assign a leaf-level variable (Ω) to model its condition, whose prior distribution is P_{Ω}^0 . Consequently, there is only one middle-level variable (S itself) for modeling the sparsity. **For** L , we first decompose it into a middle-level variable (L_1), and then recursively perform such decomposition on the sub-level variables, *i.e.*, from L_2 to L_{n-1} , until no more sub-component can be applied. This results in a hierarchical structure with L_{n-1} as the final middle-level variable. Similar to S , we introduce the condition of L_{n-1} using a leaf-level variable Γ , whose prior distribution is P_{Γ}^0 . As a result, the modeling of L involves n levels of middle-level variables, where $n \geq 2$, along with a leaf-level variable.

The above-mentioned three types of levels, *i.e.*, 0, 1 and $n(n \geq 2)$ respectively for N , S , and L , represent the three common scenarios one would encounter for modeling of decomposition. The details of our image decomposition, modeling, and the assignment of prior distributions for leaf-level variables, will be elaborated on in Section 3.2.

For convenience, we use \mathcal{Z} to denote the set of non-observation variables, representing decomposed components, *i.e.*, $\mathcal{Z} = \{L, L_1, \dots, L_{n-1}, S, \Gamma, \Omega, \Upsilon, \Lambda\}$. Furthermore, we divide this variable set into two subsets, *i.e.*, the *middle-level* variable set $\mathcal{Z}_m = \{L, L_1, \dots, L_{n-1}, S\}$ and the *leaf-level* variable set $\mathcal{Z}_l = \{\Gamma, \Omega, \Upsilon, \Lambda\}$. In the next section, we describe the inference problem of these non-observation variables.

3.1.2 Formulating inference into two sub-problems

The objective of the above hierarchical modeling is to infer the posterior of each variable given an observation, *i.e.*, $p(Z|Y)$ for any $Z \in \mathcal{Z}$. Generally, these posteriors are however intractable. Therefore, we adopt the variational inference approach to approximate them with variational distribution $q_{\phi_{\mathcal{Z}}}(\mathcal{Z}|Y)$, parameterized by $\phi_{\mathcal{Z}}$. Note that in the following, we abbreviate variational distribution $q_{\phi_{\mathcal{Z}}}(\mathcal{Z}|Y)$ as $q(\mathcal{Z})$ for convenience, unless stated otherwise.

Following the mean-field theory [61], variable groups from different levels can be assumed to be independent, namely,

$$q(\mathcal{Z}) = q(\mathcal{Z}_m)q(\mathcal{Z}_l). \quad (2)$$

One can obtain variational approximations by minimizing the Kullback-Leibler (KL) divergence between $q(\mathcal{Z})$ and $p(\mathcal{Z}|Y)$, namely, $\text{KL}(q(\mathcal{Z})\|p(\mathcal{Z}|Y))$. Since $p(\mathcal{Z}|Y)$ is intractable, we instead equivalently maximize the Evidence Lower BOund (ELBO) of $\log p(Y)$ [62], namely,

$$\phi_{\mathcal{Z}}^* \in \arg \max_{\phi_{\mathcal{Z}}} \text{ELBO}(q(\mathcal{Z}); Y), \quad (3)$$

where,

$$\text{ELBO}(q(\mathcal{Z}); Y) = \mathbb{E}_{q(\mathcal{Z})}[\log p(Y|\mathcal{Z})] - \text{KL}(q(\mathcal{Z})\|p(\mathcal{Z})). \quad (4)$$

This ELBO has two parts, *i.e.*, a fidelity term on generating observations, and a KL-divergence term related to priors $p(\mathcal{Z})$. According to the partition of \mathcal{Z} , *i.e.*, $\mathcal{Z} = \mathcal{Z}_m \cup \mathcal{Z}_l$, one can further break down the two terms in Eq. (4) into more components. For example, the KL term over priors can be rewritten as follows,

$$\begin{aligned} \text{KL}[q(\mathcal{Z})\|p(\mathcal{Z})] &= \mathbb{E}_{q(\mathcal{Z}_l)}[\text{KL}(q(\mathcal{Z}_m)\|p(\mathcal{Z}_m|\mathcal{Z}_l))] \\ &\quad + \text{KL}(q(\mathcal{Z}_l)\|p(\mathcal{Z}_l)). \end{aligned} \quad (5)$$

Similarly, we can rewrite the fidelity term for specific tasks, which will be illustrated in Section 3.3.

Dividing \mathcal{Z} into two sub-sets leads to an efficient solution for the optimization problem in Eq. (3): According to Eq. (2), one can solve the problem via an alternating algorithm, resulting in two sub-problems, of which one has a closed-form solution, as Fig. 1 (b) illustrates.

Sub-problem 1: At the $[k+1]^{\text{th}}$ step, by fixing $q(\mathcal{Z}_m)$ with $\phi_{\mathcal{Z}_m}^{[k]}$, the ELBO maximization problem of Eq. (3) can be converted into a sub-problem with respect to $\phi_{\mathcal{Z}_l}$, namely,

$$\phi_{\mathcal{Z}_l}^{[k+1]} = \arg \min_{\phi_{\mathcal{Z}_l}} \ell_l(\phi_{\mathcal{Z}_l}; \phi_{\mathcal{Z}_m}^{[k]}, Y), \quad (6)$$

where,

$$\begin{aligned} \ell_l(\phi_{\mathcal{Z}_l}; \phi_{\mathcal{Z}_m}^{[k]}, Y) &= -\text{ELBO}(q(\mathcal{Z}|\phi_{\mathcal{Z}_m} = \phi_{\mathcal{Z}_m}^{[k]}; Y) \\ &= -\mathbb{E}_{q(\mathcal{Z}_l)}\mathbb{E}_{q^{[k]}(\mathcal{Z}_m)}[\log p(Y|\mathcal{Z})] \\ &\quad + \mathbb{E}_{q(\mathcal{Z}_l)}[\text{KL}(q^{[k]}(\mathcal{Z}_m)\|p(\mathcal{Z}_m|\mathcal{Z}_l))] \\ &\quad + \text{KL}(q(\mathcal{Z}_l)\|p(\mathcal{Z}_l)) + \text{const}. \end{aligned} \quad (7)$$

Here, $q^{[k]}(\mathcal{Z}_m) = q_{\phi_{\mathcal{Z}_m}^{[k]}}(\mathcal{Z}_m)$. By selecting proper priors for leaf-level variables \mathcal{Z}_l , *i.e.*, $P_{\mathcal{Z}_l}^0$, one can obtain a closed-form solution to this problem, denoted as $\mathcal{F}_{\mathcal{Z}_l}(P_{\mathcal{Z}_l}^0, \phi_{\mathcal{Z}_m}^{[k]}, Y)$. This is the reason we use the equality sign in Eq. (6). Section 3.3 will illustrate the solution in detail.

Sub-problem 2: By fixing $q(\mathcal{Z}_l)$ with $\phi_{\mathcal{Z}_l}^{[k+1]}$, the problem of Eq. (3) becomes,

$$\phi_{\mathcal{Z}_m}^{[k+1]} \in \arg \min_{\phi_{\mathcal{Z}_m}} \ell_m(\phi_{\mathcal{Z}_m}; \phi_{\mathcal{Z}_l}^{[k+1]}, Y), \quad (8)$$

where,

$$\begin{aligned} \ell_m(\phi_{\mathcal{Z}_m}; \phi_{\mathcal{Z}_l}^{[k+1]}, Y) &= -\text{ELBO}(q(\mathcal{Z}|\phi_{\mathcal{Z}_l} = \phi_{\mathcal{Z}_l}^{[k+1]}; Y) \\ &= -\mathbb{E}_{q^{[k+1]}(\mathcal{Z}_l)}\mathbb{E}_{q(\mathcal{Z}_m)}[p(Y|\mathcal{Z})] + \text{const} \\ &\quad + \mathbb{E}_{q^{[k+1]}(\mathcal{Z}_l)}[\text{KL}(q(\mathcal{Z}_m)\|p(\mathcal{Z}_m|\mathcal{Z}_l))]. \end{aligned} \quad (9)$$

For this problem, conventionally one needs to use an iterative optimization algorithm, such as gradient descent, to minimize the objective for each observation. Here, we instead propose to adopt a neural network to learn the mapping from any observation to its corresponding solution. *This is the motivation for us to develop the next step, namely, the deep inference framework.*

3.1.3 Deep inference via neural network f_θ

We introduce a DNN, f_θ , parameterized by θ , to infer $q(\mathcal{Z})$ given any observation Y ,

$$\phi_{\mathcal{Z}} := f_\theta(Y), \forall Y \in \mathcal{Y}. \quad (10)$$

The problem in Eq. (3) then can be converted to an expected form, as follows,

$$\phi_{\mathcal{Z}}^* \in \arg \max_{\phi_{\mathcal{Z}}} \text{ELBO}(q_{\phi_{\mathcal{Z}}}(\mathcal{Z}); Y) \quad (11a)$$

↓ (converted to)

$$\theta^* \in \cap_{Y \in \mathcal{Y}} \arg \max_{\theta} \text{ELBO}(q_{f_\theta(Y)}(\mathcal{Z}); Y), \quad (11b)$$

where $\phi_{\mathcal{Z}}^* = f_{\theta^*}(Y), \forall Y \in \mathcal{Y}$

↓ (relaxed to)

$$\theta^* \in \arg \min_{\theta} \mathcal{L}_{\text{dnn}}(f_\theta; p(Y)), \quad (11c)$$

where $\phi_{\mathcal{Z}}^* \approx f_{\theta^*}(Y), \forall Y \in \mathcal{Y}$.

Here,

$$\begin{aligned} \mathcal{L}_{\text{dnn}} &= \mathbb{E}_{p(Y)} [-\text{ELBO}(q_{f_\theta(Y)}(\mathcal{Z}); Y)] \\ &= \mathbb{E}_{p(Y)} \{ \mathbb{E}_{q(\mathcal{Z})} [-\log p(Y|\mathcal{Z})] \} + \mathbb{E}_{p(Y)} [\text{KL}(q(\mathcal{Z})\|p(\mathcal{Z}))], \end{aligned} \quad (12)$$

which is the loss function for a DNN, *i.e.*, f_θ . The rationale of relaxation from Eq. (11b) to (11c) lies in the fact that θ^* is an optimal solution to the optimization problem in Eq. (11c), but not vice versa.

The architecture of f_θ following the PGM: To achieve such a DNN f_θ , which computes variational (marginal) posteriors given any observation, we propose to adopt an architecture-modularized neural network, following the structure of PGM in the first step. As illustrated in Fig. 1 (c), f_θ first infers L and S by predicting their distribution parameters $\phi_{\mathcal{Z}_m}^{[k]}$ to accomplish decomposition, and then addresses the variables in \mathcal{Z}_l . As the distribution parameters of \mathcal{Z}_l can be directly computed using a closed-form mapping $\mathcal{F}_{\mathcal{Z}_l}$ given $\phi_{\mathcal{Z}_m}^{[k]}$, we simplify f_θ to estimate only $\phi_{\mathcal{Z}_m}$, thus convert Eq. (10) to $\phi_{\mathcal{Z}_m} = f_\theta(Y)$.

Training f_θ via the inference optimization problem: The training loss of DNN f_θ is the variational objective in Eq. (12), *i.e.*, the expectation of the negative ELBO in Eq. (3). Hence, the two sub-problem formulations are applicable here, leading to a simplified training loss from sub-problem 2, since sub-problem 1 has a closed-form solution,

$$\theta^* \in \arg \min_{\theta} \mathcal{L}_{\text{dnn}}, \quad (13)$$

where the loss is as follows at the $[k+1]^{\text{th}}$ iteration,

$$\mathcal{L}_{\text{dnn}} = \mathbb{E}_{p(Y)} \left[\ell_m(\phi_{\mathcal{Z}_m} = f_\theta(Y); \phi_{\mathcal{Z}_l}^{[k+1]}, Y) \right]. \quad (14)$$

Here $\phi_{\mathcal{Z}_l}^{[k+1]}$ upon a sample Y is computed using the closed-form solution to Eq. (7), namely, $\phi_{\mathcal{Z}_l}^{[k+1]} = \mathcal{F}_{\mathcal{Z}_l}(P_{\mathcal{Z}_l}^0, \phi_{\mathcal{Z}_m}^{[k]}, Y)$, where $\phi_{\mathcal{Z}_m}^{[k]}$ are computed via the forward inference with the current DNN parameter $\theta^{[k]}$, *i.e.*, $\phi_{\mathcal{Z}_m}^{[k]} = f_{\theta^{[k]}}(Y)$ for a sample Y . Once computed, detached $\phi_{\mathcal{Z}_l}^{[k+1]}$ is used for the calculation of the loss function Eq. (14) to update θ . Hence, for the current batch $\mathcal{D}_B = \{Y^{(i)}\}_{i=1}^{|\mathcal{D}_B|}$ at the $[k+1]^{\text{th}}$ iteration, the training loss of DNN f_θ becomes,

$$\hat{\mathcal{L}}_{\text{dnn}} = \frac{1}{|\mathcal{D}_B|} \sum_{i=1}^{|\mathcal{D}_B|} [\ell_m(f_\theta(Y^{(i)}); \phi_{\mathcal{Z}_l}^{(i)[k+1]}, Y^{(i)})]. \quad (15)$$

where $\phi_{\mathcal{Z}_l}^{(i)[k+1]} = \mathcal{F}_{\mathcal{Z}_l}(P_{\mathcal{Z}_l}^0, f_{\theta^{[k]}}(Y^{(i)}), Y^{(i)})$. *This loss leads to strong generalizability, which will be elaborated on in the following interpretation.*

3.1.4 Interpretation

Interpretability and modularity of f_θ : In this DNN, each module corresponds to a decomposition step from the hierarchical model, with inputs, outputs, and functions aligned with the HBM. The loss function \mathcal{L}_{dnn} captures the dependencies between modules through output computation, offering clear interpretability. Section 3.2 to 3.4 detail this interpretation using an image decomposition task.

Generalizability of f_θ : The introduction of hierarchical Bayesian modeling, which incorporates prior knowledge of variables and their interactions, establishes assumptions (preferences) about the solutions for the algorithm. This approach encourages the algorithm to prioritize certain solutions and is a potential method to achieve generalizability with a finite training set, as the no-free-lunch theorem says [63]–[65]. Below are two concrete explanations.

Firstly, the framework meets the PAC-Bayesian theory, which naturally guarantees a generalization error bound for f_θ [22], [23], since the design of f_θ is conducted by HBM. We will provide a detailed illustration of this in Section 3.5.

Secondly, one can see that the KL-divergence term in Eq. (9), *i.e.*, $\mathbb{E}_{q^{[k+1]}(\mathcal{Z}_l)} [\text{KL}(q(\mathcal{Z}_m)\|p(\mathcal{Z}_m|\mathcal{Z}_l))]$, can be treated as a *stochastic regularization term*. Specifically, the KL divergence is stochastically disturbed by $q^{[k+1]}(\mathcal{Z}_l)$ computed in forward-propagation from the current DNN at $[k+1]^{\text{th}}$ iteration. Different from a common prior for \mathcal{Z}_m , *e.g.* $p(\mathcal{Z}_m) = \mathcal{N}(0, 1)$, the hierarchical modeling, $p(\mathcal{Z}_m|\mathcal{Z}_l)$ introduces the stochastic optimization with randomly turbulent objective functions during training, which helps the training procedure escape from local optima and consequently enhances the generalizability of the resulting DNN.

3.2 Hierarchical Bayesian modeling of decomposition

In this section, we elaborate on the modeling details. We specify the PGM and model each variable in \mathcal{Z} with dedicated priors. Note that we may need to introduce new variables to the PGM or need to prune it, resulting in a new PGM in Fig. 2 (a). For convenience, we illustrate the modeling of these variables according to separate branches in Fig. 1 (a), namely, (1) variables $\{L, \dots, \Gamma\}$ related to the low-rank modeling, (2) variables $\{S, \Omega\}$ related to the sparsity modeling, and (3) variables $\{N, \Upsilon, \Lambda\}$ related to noise. Particularly, conjugate priors are adopted to ensure

the variational posteriors belong to the same distribution family as the priors.

To model the low-rank variable (L), we decompose it into two middle-level variables, *i.e.*, the left factor (denoted as A) and the right factor (denoted as B^T). Let $A = [\mathbf{a}_1, \dots, \mathbf{a}_{r^0}]$ and $B^T = [\mathbf{b}_1, \dots, \mathbf{b}_{r^0}]^T$, where vectors $\mathbf{a}_i \in \mathbb{R}^h$, $\mathbf{b}_i \in \mathbb{R}^w$ and r^0 is a hyper-parameter; we then rewrite L , as follows,

$$L = AB^T = \sum_{i=1}^{r^0} \mathbf{a}_i \times \mathbf{b}_i^T = \sum_{i=1}^{r^0} O_i. \quad (16)$$

Hence, the rank of A or B is no more than r^0 , namely $\text{rank}(A) \leq r^0$, $\text{rank}(B) \leq r^0$, and $\text{rank}(L) \leq r^0$. The rank of the matrix $O_i = (\mathbf{a}_i \times \mathbf{b}_i^T)$ is equal to 1 if and only if both \mathbf{a}_i and \mathbf{b}_i are non-zero vectors. Hence, the rank of L is bounded by the number of rank-one matrices ($\{O_i\}$). Therefore, one can achieve the low-rank constraint by controlling the number of non-zero vectors in A and B . Specifically, we introduce a leaf-level variable $\gamma \in \mathbb{R}^{r^0}$ to control A and B simultaneously for compact modeling [8], as Fig. 2 (a) shows, namely,

$$p(A|\gamma) = \prod_{i=1}^{r^0} \mathcal{N}(\mathbf{a}_i|0, \gamma_i^{-1}I_h), \quad (17)$$

$$p(B|\gamma) = \prod_{i=1}^{r^0} \mathcal{N}(\mathbf{b}_i|0, \gamma_i^{-1}I_w), \quad (18)$$

where I_h refers to the $h \times h$ identity matrix. One can see that if the i -th element of γ , namely γ_i , tends to be infinity, the controlled columns \mathbf{a}_i and \mathbf{b}_i tend to be zero vectors and O_i tends to be a zero matrix, resulting in a lower rank of L . Hence, the rank of L can be regularized by γ . We further assign a conjugate prior to γ , as follows,

$$p(\gamma|\alpha_\gamma^0, \beta_\gamma^0) = \prod_{i=1}^{r^0} \mathcal{G}(\gamma_i|\alpha_\gamma^0, \beta_\gamma^0), \quad (19)$$

where, $\mathcal{G}(\cdot, \cdot)$ denotes Gamma distribution, with hyper-parameters α_γ^0 and $\beta_\gamma^0 \in \mathbb{R}$. Note that, under the above modeling, the variable L is deterministically dependent on A and B , namely, $p(L = A \times B^T|A, B) = 1$. Hence, we denote it with a dotted circle in the PGM of Fig. 2(a), meaning that it can be pruned.

To ensure the sparsity of S , we utilize $\Omega \in \mathbb{R}^{h \times w}$ to independently model the elements of S , as follows,

$$p(S|\Omega) = \prod_{i=1, j=1}^{h, w} \mathcal{N}(s_{ij}|0, \omega_{ij}^{-1}). \quad (20)$$

One can see that when ω_{ij} tends to infinity, the corresponding element s_{ij} statistically approaches zero as well. Moreover, we impose a conjugate prior on Ω ,

$$p(\Omega|\alpha_\omega^0, \beta_\omega^0) = \prod_{i=1, j=1}^{h, w} \mathcal{G}(\omega_{ij}|\alpha_\omega^0, \beta_\omega^0), \quad (21)$$

where α_ω^0 and $\beta_\omega^0 \in \mathbb{R}$ are hyper-parameters. Note that the marginal distribution $p(S) = \int p(S|\Omega)p(\Omega)d\Omega$ is a Student's t -distribution, which has been widely utilized to model sparsity [66].

To model the noise (N), we assume that the noise follows a pixel-wise normal distribution with mean 0 and the inverse variance λ_{ij} . Here, we use a matrix $\Lambda = [\lambda_{ij}]_{h \times w}$,

TABLE 2: Priors and variational distributions for variables.

$p(\mathcal{Z})$	$q(\mathcal{Z})$
$p(A \gamma) := \prod_{i=1}^{r^0} \mathcal{N}(\mathbf{a}_i 0, I_h/\gamma_i)$	$q(A) := \prod_{i=1}^{r^0} \mathcal{N}(\mathbf{a}_i \mu_{\mathbf{a}_i}, \text{diag}(\sigma_{\mathbf{a}_i}^2))$
$p(B \gamma) := \prod_{i=1}^{r^0} \mathcal{N}(\mathbf{b}_i 0, I_w/\gamma_i)$	$q(B) := \prod_{i=1}^{r^0} \mathcal{N}(\mathbf{b}_i \mu_{\mathbf{b}_i}, \text{diag}(\sigma_{\mathbf{b}_i}^2))$
$p(S \Omega) := \prod_{i,j=1}^{h,w} \mathcal{N}(s_{ij} 0, 1/\omega_{ij})$	$q(S A, B) := \prod_{i,j=1}^{h,w} \mathcal{N}(s_{ij} \mu_{s_{ij}}, \sigma_{s_{ij}}^2)$
$p(\gamma \alpha_\gamma^0, \beta_\gamma^0) := \prod_{i=1}^{r^0} \mathcal{G}(\gamma_i \alpha_\gamma^0, \beta_\gamma^0)$	$q(\gamma) := \prod_{i=1}^{r^0} \mathcal{G}(\gamma_i \alpha_{\gamma_i}, \beta_{\gamma_i})$
$p(\Omega \alpha_\omega^0, \beta_\omega^0) := \prod_{i,j=1}^{h,w} \mathcal{G}(\omega_{ij} \alpha_\omega^0, \beta_\omega^0)$	$q(\Omega) := \prod_{i,j=1}^{h,w} \mathcal{G}(\omega_{ij} \alpha_{\omega_{ij}}, \beta_{\omega_{ij}})$
$p(\Lambda \alpha_\lambda^0, \beta_\lambda^0) := \prod_{i,j=1}^{h,w} \mathcal{G}(\lambda_{ij} \alpha_\lambda^0, \beta_\lambda^0)$	$q(\Lambda) := \prod_{i,j=1}^{h,w} \mathcal{G}(\lambda_{ij} \alpha_{\lambda_{ij}}, \beta_{\lambda_{ij}})$

referred to as pixel-wise precision matrix, to denote all λ_{ij} , thus $p(N|\Lambda) = \prod_{i=1, j=1}^{h \times w} \mathcal{N}(n_{ij}|0, \lambda_{ij}^{-1})$. To model Λ , we impose a conjugate prior,

$$p(\Lambda|\alpha_\lambda^0, \beta_\lambda^0) = \prod_{i=1, j=1}^{h, w} \mathcal{G}(\lambda_{ij}|\alpha_\lambda^0, \beta_\lambda^0). \quad (22)$$

Here, pixel-wise λ_{ij} follows the Gamma distribution with a shape parameter $\alpha_\lambda^0 \in \mathbb{R}$ and an inverse scale parameter $\beta_\lambda^0 \in \mathbb{R}$.

Moreover, to facilitate a task-specific decomposition, we introduce another observation, namely, the target variable $U = [u_{ij}]_{h \times w}$. Specifically, U refers to the information dependent on the noise-free components. We will instantiate the modeling of U for specific tasks in Section 3.6.

Fig. 2 (a) illustrates the compact PGM w.r.t. variables $\mathcal{Z} = \{A, B, S, \gamma, \Omega, \Lambda\}$ given observations $\{Y, U\}$. Based on this PGM, we adjust the middle-level variable set to $\mathcal{Z}_m = \{A, B, S\}$ and the leaf-level variable set to $\mathcal{Z}_l = \{\gamma, \Omega, \Lambda\}$.

3.3 Convert inference into two optimizations via VI

In this section, we elaborate on the details of the optimization problem conducted via variational inference for \mathcal{Z} , as Section 3.1.2 briefs.

Similar to Eq. (2), we assume the variational distribution $q(\mathcal{Z})$ to be expressed as,

$$q(\mathcal{Z}) = q(A)q(B)q(S|A, B)q(\gamma)q(\Omega)q(\Lambda). \quad (23)$$

To enable tractable computation of KL-divergence terms in ELBO, we further assume that $q(\mathcal{Z})$ follows the same form of the conjugate priors assigned to \mathcal{Z} , as summarized in Table 2. Specifically, for each middle-level variable $Z \in \mathcal{Z}_m = \{A, B, S\}$, the variational distribution $q(Z)$ follows the Gaussian distributions with unknown mean-variance parameters $\phi_Z = \{\mu_Z, \sigma_Z\}$, *e.g.*, $q(A) = \prod_{i=1}^{r^0} \mathcal{N}(\mathbf{a}_i|\mu_{\mathbf{a}_i}, \text{diag}(\sigma_{\mathbf{a}_i}^2))$ with parameters $\phi_A = \{\mu_A, \sigma_A\}$, where $\mu_A = [\mu_{\mathbf{a}_1}, \dots, \mu_{\mathbf{a}_{r^0}}] \in \mathbb{R}^{h \times r^0}$ and $\sigma_A = [\sigma_{\mathbf{a}_1}, \dots, \sigma_{\mathbf{a}_{r^0}}] \in \mathbb{R}^{h \times r^0}$. Then, we have the parameter set $\phi_{\mathcal{Z}_m} = \{\mu_A, \sigma_A, \mu_B, \sigma_B, \mu_S, \sigma_S\}$. Similarly, for each leaf-level variable $Z \in \mathcal{Z}_l = \{\gamma, \Omega, \Lambda\}$, $q(Z)$ follows the Gamma distribution with parameters $\phi_Z = \{\alpha_Z, \beta_Z\}$, *e.g.*, $q(\gamma) = \prod_{i=1}^{r^0} \mathcal{G}(\gamma_i|\alpha_{\gamma_i}, \beta_{\gamma_i})$ with parameters $\phi_\gamma = \{\alpha_\gamma, \beta_\gamma\}$. Hence, the variational parameter set for \mathcal{Z}_l is now $\phi_{\mathcal{Z}_l} = \{\alpha_\gamma, \beta_\gamma, \alpha_\Omega, \beta_\Omega, \alpha_\Lambda, \beta_\Lambda\}$.

Based on the new PGM in Fig. 2 (a), when given observations $\{Y, U\}$, the objective of negative ELBO in Eq. (4) can

be reformulated as,

$$\begin{aligned} \ell(Y, U) &= -\text{ELBO}(q(\mathcal{Z}); Y, U) \\ &= -\mathbb{E}_{q(\mathcal{Z})}[\log p(Y|\mathcal{Z})] \quad (\text{fidelity term: } \ell_{fid}) \end{aligned} \quad (24a)$$

$$- \mathbb{E}_{q(\mathcal{Z}_m)}[\log p(U|\mathcal{Z}_m)] \quad (\text{supervision term: } \ell_{sup}) \quad (24b)$$

$$+ \underbrace{\mathbb{E}_{q(\gamma)}[\text{KL}(q(A)q(B)\|p(A|\gamma)p(B|\gamma))]}_{(\text{low-rank term: } \ell_{rank})} \quad (24c)$$

$$+ \underbrace{\mathbb{E}_{q(\Omega)}\mathbb{E}_{q(A,B)}[\text{KL}(q(S|A, B)\|p(S|\Omega))]}_{(\text{sparsity term: } \ell_{sparse})} \quad (24d)$$

$$+ \text{KL}(q(\gamma)\|p(\gamma)) \quad (\gamma\text{-prior term: } \ell_\gamma) \quad (24e)$$

$$+ \text{KL}(q(\Omega)\|p(\Omega)) \quad (\Omega\text{-prior term: } \ell_\Omega) \quad (24f)$$

$$+ \text{KL}(q(\Lambda)\|p(\Lambda)) \quad (\Lambda\text{-prior term: } \ell_\Lambda). \quad (24g)$$

where the terms on the right side are denoted as ℓ_{fid} , ℓ_{sup} , ℓ_{rank} , ℓ_{sparse} , ℓ_γ , ℓ_Ω , and ℓ_Λ , respectively. Concretely, ℓ_{fid} imposes the consistency between the generated data from the posterior distributions and the observation Y , and ℓ_{sup} drives the generated data to be task-specific targets supervised by the ground truth U . Moreover, ℓ_{rank} constrains the low-rank property of variable L , and ℓ_{sparse} enforces variable S to be sparse. Finally, ℓ_γ , ℓ_Ω , and ℓ_Λ penalize the distance between variational approximations and priors of their corresponding variables.

To minimize Eq. (24) w.r.t. $\phi_{\mathcal{Z}}$, we split the objective function and derive two sub-problems, *i.e.*, **sub-problem 1** w.r.t. the leaf-level variable set $\mathcal{Z}_l = \{\gamma, \Omega, \Lambda\}$ and **sub-problem 2** w.r.t. the middle-level variable set $\mathcal{Z}_m = \{A, B, S\}$, as Section 3.1.2 briefs. In the following, we first illustrate closed-form solutions to sub-problem 1 in Section 3.3.1 and then elaborate on the objective function for sub-problem 2 in Section 3.3.2.

3.3.1 Closed-form solutions for sub-problem 1

At the $[k+1]^{\text{th}}$ iteration, given $\phi_{\mathcal{Z}_m}^{[k]}$ for $q(\mathcal{Z}_m)$ and the specific assignments in Table 2, one can obtain a closed-form solution $\phi_{\mathcal{Z}_l}^{[k+1]}$ to the problem defined in Eq. (6), *i.e.*, minimizing $\ell_l(\phi_{\mathcal{Z}_l}; \phi_{\mathcal{Z}_m}^{[k]}, Y)$ (abbreviated as ℓ_l), to update $q(\mathcal{Z}_l)$. Specifically, after substituting the ELBO in Eq. (24) into Eq. (7), ℓ_l consists of six terms, *i.e.*, ℓ_{fid} , ℓ_{rank} , ℓ_{sparse} , ℓ_γ , ℓ_Ω , and ℓ_Λ in Eq. (24), since ℓ_{sup} is constant. Moreover, due to the independence between γ , Ω , and Λ , their variational distributions can be optimized separately. In the following, we provide the expressions of these solutions, while *details of the deduction for their closed-form solutions can be found in Section 1 of Supplementary Material*. Note that the iteration index denoted with superscript $[k]$ will be omitted here for brevity.

For variable γ , minimizing ℓ_l over $q(\gamma)$ is equivalent to minimizing

$$\ell_l(\phi_\gamma; \phi_A, \phi_B) = \ell_{rank} + \ell_\gamma, \quad (25)$$

which is only related to $\phi_A = \{\mu_A, \sigma_A\}$ and $\phi_B = \{\mu_B, \sigma_B\}$. The closed-form solution for each element in ϕ_γ , *i.e.*, $\alpha_{\gamma_i}, \beta_{\gamma_i}$, can be derived,

$$\begin{cases} \alpha_{\gamma_i} = 2\alpha_\gamma^0 + h + w \\ \beta_{\gamma_i} = 2\beta_\gamma^0 + \|\mu_{a_i}\|_2^2 + \|\sigma_{a_i}\|_2^2 + \|\mu_{b_i}\|_2^2 + \|\sigma_{b_i}\|_2^2. \end{cases} \quad (26)$$

Since $q(\gamma_i)$ is a Gamma distribution, we have $\mu_{\gamma_i} = \mathbb{E}[\gamma_i] = \alpha_{\gamma_i}/\beta_{\gamma_i}$. Note that μ_{γ_i} tends to be a larger value when β_{γ_i} is smaller, which subsequently encourages a_i and b_i to approach zero, resulting in a lower rank for L .

For variable Ω , minimizing ℓ_l over $q(\Omega)$ is equivalent to minimizing

$$\ell_l(\phi_\Omega; \phi_S) = \ell_{sparse} + \ell_\Omega, \quad (27)$$

which is only conditioned on $\phi_S = \{\mu_S, \sigma_S\}$. Then, the closed-form solution for each element in ϕ_Ω , *i.e.*, $\alpha_{\omega_{ij}}, \beta_{\omega_{ij}}$, is given by,

$$\begin{cases} \alpha_{\omega_{ij}} = 2\alpha_\omega^0 + 1, \\ \beta_{\omega_{ij}} = 2\beta_\omega^0 + \mu_{s_{ij}}^2 + \sigma_{s_{ij}}^2. \end{cases} \quad (28)$$

Similarly, we have $\mu_{\omega_{ij}} = \mathbb{E}[\omega_{ij}] = \alpha_{\omega_{ij}}/\beta_{\omega_{ij}}$. When $\beta_{\omega_{ij}}$ is smaller, $\mu_{\omega_{ij}}^{-1}$ tends to drive s_{ij} zero, leading to a sparser S .

For variable Λ , minimizing ℓ_l over $q(\Lambda)$ is equivalent to minimizing

$$\ell_l(\phi_\Lambda; \phi_{\mathcal{Z}_m}, Y) = \ell_{fid} + \ell_\Lambda. \quad (29)$$

The closed-form solution for each element in ϕ_Λ , *i.e.*, $\alpha_{\lambda_{ij}}$ and $\beta_{\lambda_{ij}}$, is as follows,

$$\begin{cases} \alpha_{\lambda_{ij}} = 2\alpha_\lambda^0 + 1, \\ \beta_{\lambda_{ij}} = 2\beta_\lambda^0 + [y_{ij} - (\sum_k^r \hat{a}_{ik} \times \hat{b}_{jk} + \hat{s}_{ij})]^2, \end{cases} \quad (30)$$

where $[\hat{a}_{ik}]_{h \times r^0} = \hat{A}$, $[\hat{b}_{jk}]_{w \times r^0} = \hat{B}$ and $[\hat{s}_{ij}]_{h \times w} = \hat{S}$ are sampled from $q(A)$, $q(B)$ and $q(S|A, B)$, which will be illustrated in the following section. Similarly, we have $\mu_{\lambda_{ij}} = \mathbb{E}[\lambda_{ij}] = \alpha_{\lambda_{ij}}/\beta_{\lambda_{ij}}$. The smaller residual error in the denominator leads to the larger value of $\mu_{\lambda_{ij}}$, resulting in a weaker noise level of n_{ij} in N .

3.3.2 The objective function for sub-problem 2

By fixing $q(\mathcal{Z}_l)$ with $\phi_{\mathcal{Z}_l}^{[k+1]}$, we need to update $q(\mathcal{Z}_m)$ by minimizing $\ell_m(\phi_{\mathcal{Z}_m}; \phi_{\mathcal{Z}_l}^{[k+1]}, Y)$, as defined in Eq. (8). After substituting the ELBO in Eq. (24) into Eq. (9), the objective function ℓ_m w.r.t. $\phi_{\mathcal{Z}_m}$ can be expressed by,

$$\ell_m(\phi_{\mathcal{Z}_m}; \phi_{\mathcal{Z}_l}, Y, U) = \ell_{fid} + \ell_{sup} + \ell_{rank} + \ell_{sparse} + \text{const}, \quad (31)$$

since the prior terms related to \mathcal{Z}_l , *i.e.*, ℓ_γ , ℓ_Ω , and ℓ_Λ in Eq. (24), are constant given $q(\mathcal{Z}_l)$.

For the fidelity term ℓ_{fid} , it is intractable to compute the expectation directly. Hence, we apply the following equivalent expression and approximate it with the Monte Carlo sampling strategy [67],

$$\begin{aligned} \ell_{fid} &= -\mathbb{E}_{q(\mathcal{Z})}[\log p(Y|\mathcal{Z})] = -\mathbb{E}_{q(\Lambda)}[\mathbb{E}_{q(\mathcal{Z}|\Lambda)} \log p(Y|\mathcal{Z})] \\ &\approx \frac{1}{2} \left\| \sqrt{\mu_\Lambda} \odot (Y - (\hat{A}\hat{B}^T + \hat{S})) \right\|_F^2. \end{aligned} \quad (32)$$

Here, we adopt the reparameterization technique [67], and have $\hat{A} = \mu_A + \sigma_A \odot \eta$, $\hat{B} = \mu_B + \sigma_B \odot \eta$, and $\hat{S} = \mu_S + \sigma_S \odot \eta$, where $\eta \sim \mathcal{N}(\mathbf{0}, \mathbf{I})$. Moreover, the supervision term ℓ_{sup} in Eq. (24) is task-specific which will be instantiated in Section 3.6.

The low-rank term ℓ_{rank} can be expressed as a function w.r.t. parameters of $q(A)$ and $q(B)$, namely, $\phi_A = \{\mu_A, \sigma_A\}$

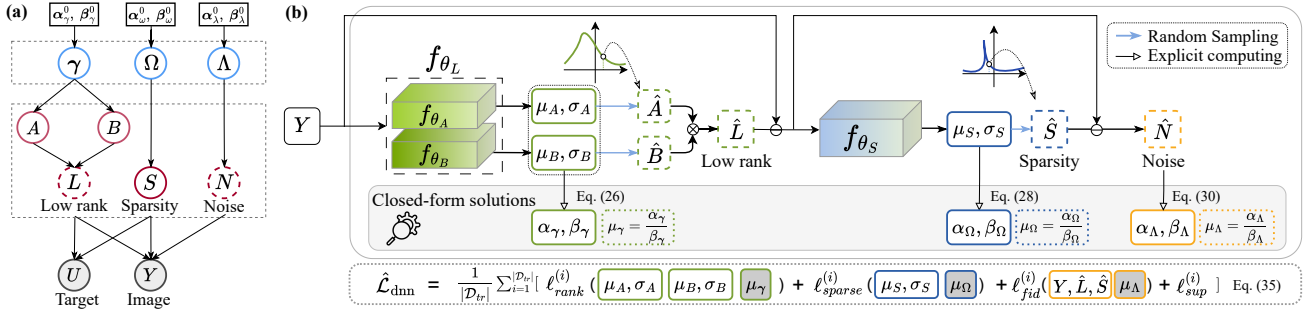


Fig. 2: The PGM and architecture of InDeed. (a) illustrates the PGM with observation variables $\{Y, U\}$ and non-observation $\mathcal{Z} = \{A, B, S, \gamma, \Omega, \Lambda\}$. No inference is required for variables L and N in dotted circles. (b) shows the architecture. Given an observation Y , the posteriors of middle-level variables, *i.e.*, A, B and S , are first inferred via neural networks, and then the expectations of leaf-level variables, *i.e.*, μ_γ, μ_Ω and μ_Λ , are given by the closed-form solutions in Eq. (26), Eq. (28), and Eq. (30), respectively. The shaded parameters are detached values during training.

and $\phi_B = \{\mu_B, \sigma_B\}$, given the updated expectation of γ ($\mu_\gamma = \mathbb{E}[\gamma] = \alpha_\gamma / \beta_\gamma$ using Eq. (26)),

$$\ell_{\text{rank}} = \frac{1}{2} \left\{ \|\mu_A \odot \mathbf{1}_h \sqrt{\mu_\gamma}^T\|_F^2 + \langle \mathbf{1}_h \mu_\gamma^T, \sigma_A^2 \rangle_F - \langle \mathbf{1}_h \times r^0, \ln \sigma_A^2 \rangle_F \right. \\ \left. + \|\mu_B \odot \mathbf{1}_w \sqrt{\mu_\gamma}^T\|_F^2 + \langle \mathbf{1}_w \mu_\gamma^T, \sigma_B^2 \rangle_F - \langle \mathbf{1}_w \times r^0, \ln \sigma_B^2 \rangle_F \right\}, \quad (33)$$

where \odot refers to Hadamard product and $\mathbf{1}_x$ is a vector or matrix of ones with shape x .

Similarly, the sparsity term ℓ_{sparse} can be expressed as a function w.r.t. parameters of $q(S)$, namely $\phi_S = \{\mu_S, \sigma_S\}$, given the updated expectation of Ω ($\mu_\Omega = \mathbb{E}[\Omega] = \alpha_\Omega / \beta_\Omega$ using Eq. (28)),

$$\ell_{\text{sparse}} = \frac{1}{2} \left\{ \|\mu_S \odot \sqrt{\mu_\Omega}\|_F^2 + \langle \mu_\Omega, \sigma_S^2 \rangle_F - \langle \mathbf{1}_{h \times w}, \ln \sigma_S^2 \rangle_F \right\}. \quad (34)$$

As Section 3.1.3 briefs, we propose to build a neural network to infer the solutions instead of individually optimizing $\phi_{\mathcal{Z}_m}$ for each observation, which will be illustrated in the next section.

3.4 InDeed: Deep inference

In this section, we elaborate on details of the proposed interpretable deep decomposition inference method, *i.e.*, InDeed, including the objective function, the architecture, and the interpretation.

3.4.1 Objective function

Given a training data set $\mathcal{D}_{tr} = \{Y^{(i)}, U^{(i)}\}_{i=1}^{|\mathcal{D}_{tr}|}$, the objective function of f_θ , namely, the empirical version of Eq. (14) can be expressed as, combining Eq. (31),

$$\hat{\mathcal{L}}_{\text{dnn}} = \frac{1}{|\mathcal{D}_{tr}|} \sum_{i=1}^{|\mathcal{D}_{tr}|} \left[\ell_m(\phi_{\mathcal{Z}_m} = f_\theta(Y^{(i)}); \phi_{\mathcal{Z}_l}^{[k+1]}, Y^{(i)}, U^{(i)}) \right] \\ = \frac{1}{|\mathcal{D}_{tr}|} \sum_{i=1}^{|\mathcal{D}_{tr}|} [\ell_{\text{fid}}^{(i)} + \ell_{\text{sup}}^{(i)} + \ell_{\text{rank}}^{(i)} + \ell_{\text{sparse}}^{(i)}] + \text{const}, \quad (35)$$

where $\ell_*^{(i)}$ refers to the corresponding loss computed for the i -th sample, as illustrated in Section 3.3.2.

3.4.2 Architecture

Following the framework illustrated in Fig. 1 (c), we develop a modularized neural network for InDeed, as Fig. 2 (b) shows. According to Eq. (23), we infer the variational posteriors of A and B in parallel to obtain L , followed by the estimation of the posterior of S . The noise component (N) can be computed directly based on the image decomposition. Hence, InDeed consists of two major modules, *i.e.*, f_{θ_L} and f_{θ_S} , respectively for the low-rank and sparsity representation, and f_{θ_L} is composed of two sub-modules.

For the low-rank component, we design the low-rank module f_{θ_L} with two parallel sub-modules f_{θ_A} and f_{θ_B} , following the modeling of $L = AB^T$ in Eq. (16). These sub-modules aim to estimate distribution parameters w.r.t. $q(A)$ and $q(B)$, namely $\phi_A = \{\mu_A, \sigma_A\} := f_{\theta_A}(Y)$ and $\phi_B = \{\mu_B, \sigma_B\} := f_{\theta_B}(Y)$. Specifically, to implement the low-rank expression in Eq. (16), f_{θ_A} is designed to learn the mapping from the image space to the Cartesian product of $2r^0$ vector spaces, $\mathbb{R}^{h \times w} \rightarrow \prod_{i=1}^{2r^0} \mathbb{R}^{h \times 1}$, and outputs two sets of r^0 column vectors, for μ_A and σ_A , respectively. Similarly, $f_{\theta_B} : \mathbb{R}^{h \times w} \rightarrow \prod_{i=1}^{2r^0} \mathbb{R}^{1 \times w}$ outputs two sets of r^0 row vectors for μ_B^T and σ_B^T . Then, following the reparameterization technique [67], we sample \hat{A}, \hat{B} respectively from the inferred variational distributions, *i.e.*, $q(A|\mu_A, \sigma_A^2)$ and $q(B|\mu_B, \sigma_B^2)$.

For the sparsity component, we design a sparsity module $f_{\theta_S} : \mathbb{R}^{h \times w} \rightarrow \mathbb{R}^{h \times w}$ to estimate the variational parameters for $q(S|A, B)$, namely this module takes $(Y - \hat{A}\hat{B}^T)$ as inputs and outputs the corresponding parameters, *i.e.*, $\phi_S = \{\mu_S, \sigma_S\} := f_{\theta_S}(Y - \hat{A}\hat{B}^T)$.

For the noise component, it is explicitly expressed as $\hat{N} = Y - \hat{A}\hat{B}^T - \hat{S}$, where \hat{S} is sampled from $q(S|\mu_S, \sigma_S^2)$.

For variables in \mathcal{Z}_l , they are explicitly computed with Eq. (26), (28), and (30), as Fig. 2 (b) illustrates.

For the aforementioned (sub-)modules, we in practice employ ResNet [68] with group normalization as the backbone. Please refer to Section 4 in Supplementary Material for more details of the implementation.

3.4.3 Interpretation

As InDeed follows the three-step framework, its interpretability comes from two key aspects: the modularized

structure guided by the PGM and the additively separable loss function derived from variational inference.

First, InDeed's structure is partially transparent, combining closed-form solutions for leaf-level variables with modularized networks (f_θ) for middle-level variable estimation. The intermediate outputs of f_θ , such as the distribution parameters of variational posteriors $q(A)$, $q(B)$, and $q(S)$, are statistically interpretable, given their priors and \mathcal{Z}_l .

Second, the loss function $\hat{\mathcal{L}}_{\text{dnn}}$, derived from variational inference, integrates various terms mathematically, eliminating the need for manual balancing. Each term in $\hat{\mathcal{L}}_{\text{dnn}}$ reflects the information of the intermediate outputs from different aspects, enhancing the interpretability of each module.

Finally, thanks to the separability of $\hat{\mathcal{L}}_{\text{dnn}}$, we can achieve active generalization by adaptation, as Section 3.5.2 will illustrate.

3.5 Error bound and active generalization

In this section, we analyze the generalization error bound of InDeed, based on which we further develop an unsupervised test-time adaptation algorithm, for out-of-distribution (OOD) scenarios.

3.5.1 Generalization error bound

Let $p(Y)$ be the data distribution, $\mathcal{D} = \{Y^{(i)}\}_{i=1}^{|\mathcal{D}|}$ be a data set sampled from $p(Y)$, and the empirical distribution function defined on \mathcal{D} be $\hat{p}_{\mathcal{D}}(Y) = \frac{1}{|\mathcal{D}|} \sum_{i=1}^{|\mathcal{D}|} \mathbb{1}_{\{Y=Y^{(i)}\}}$. Let $\mathcal{R}(f_\theta)$ denote the expected generalization error of f_θ over $p(Y)$, defined as $\mathcal{R}(f_\theta) = \mathbb{E}_{p(Y)}\{\mathbb{E}_{q(\mathcal{Z}|Y)}[-\log p(Y|\mathcal{Z})]\}$, and the empirical error over \mathcal{D} as $\hat{\mathcal{R}}(f_\theta; \mathcal{D}) = \frac{1}{|\mathcal{D}|} \sum_{i=1}^{|\mathcal{D}|} \{\mathbb{E}_{q(\mathcal{Z}|Y^{(i)})}[-\log p(Y^{(i)}|\mathcal{Z})]\}$. Similarly, we define empirical KL over \mathcal{D} as $\hat{\text{KL}}(q, p; \mathcal{D}) = \frac{1}{|\mathcal{D}|} \sum_{i=1}^{|\mathcal{D}|} [\text{KL}(q(\mathcal{Z}|Y^{(i)})||p(\mathcal{Z}))]$. Then, based on the PAC-Bayesian theorem [22], [23], [69], we can obtain an upper bound for $\mathcal{R}(f_\theta)$ provided in Theorem 1.

Theorem 1. Let f_θ be any K_θ -Lipschitz-continuous function, and $\delta \in (0, 1)$. We then have the following inequality hold with probability at least $1 - \delta$:

$$\begin{aligned} \mathcal{R}(f_\theta) &\leq \hat{\mathcal{R}}(f_\theta; \mathcal{D}) + \hat{\text{KL}}(q, p; \mathcal{D}) \\ &\quad + K \cdot d(\hat{p}_{\mathcal{D}}(Y), p(Y)) + C. \end{aligned} \quad (36)$$

Here, $d(p_1, p_2)$ refers to the discrepancy between two distributions p_1 and p_2 , as defined in [23]; C is a constant given prior $p(\mathcal{Z})$; $K = c(K_\theta)$ is determined by K_θ .

To tighten the error bound, two primary approaches can be considered: reducing the Lipschitz constant K_θ [70], and controlling the first two terms, *i.e.*, $\hat{\mathcal{R}}(f_\theta; \mathcal{D})$ and $\hat{\text{KL}}(q, p; \mathcal{D})$. Herein, we mainly focus on the latter one.

Relation to $\hat{\mathcal{L}}_{\text{dnn}}$ of f_θ : By comparing Eq. (12) and the above-mentioned upper bound, one can see that $\hat{\mathcal{R}}(f_\theta; \mathcal{D}) + \hat{\text{KL}}(q, p; \mathcal{D})$ is the empirical version of \mathcal{L}_{dnn} over \mathcal{D} . Hence, one can rewrite this upper bound using the same notation,

$$\hat{\mathcal{L}}_{\text{dnn}}(f_\theta; \mathcal{D}) = \hat{\mathcal{R}}(f_\theta; \mathcal{D}) + \hat{\text{KL}}(q, p; \mathcal{D}). \quad (37)$$

This loss ($\hat{\mathcal{L}}_{\text{dnn}}(f_\theta; \mathcal{D})$) is equivalent to that ($\hat{\mathcal{L}}_{\text{dnn}}$) in Eq (35) excluding the supervision term (ℓ_{sup}), in the absence of target U . Hence, minimizing Eq (35) tends to reduce the error bound in Eq. (36). *This explains the good generalizability of InDeed [69] and motivates us to develop a test-time adaptation algorithm for OOD scenarios.*

3.5.2 Active generalization for OOD scenarios

We refer to this algorithm as InDeed Active Generalization (InDeedAG). Furthermore, we extend InDeedAG to InDeed Online Active Generalization (InDeedOAG) to accommodate real-world scenarios necessitating adaptation for an individual OOD image only.

Let f_{θ^*} be the model trained with \mathcal{D}_{tr} ; let \mathcal{D}_{ood} be an OOD test data set sampled from $p(Y)$. When the empirical distribution over \mathcal{D}_{ood} differs significantly from that of \mathcal{D}_{tr} , the solution of f_{θ^*} from minimization of $\hat{\mathcal{L}}_{\text{dnn}}(f_\theta; \mathcal{D}_{tr})$ can be inferior for \mathcal{D}_{ood} . To improve the solution, one can intuitively further improve the model by combining the two datasets, following Theorem 1,

$$f_{\theta_{\text{AG}}} = \arg \min_{f_\theta} \hat{\mathcal{L}}_{\text{AG}} := \hat{\mathcal{L}}_{\text{dnn}}(f_\theta; \mathcal{D}_{tr} \cup \mathcal{D}_{ood}). \quad (38)$$

Generally, reusing \mathcal{D}_{tr} is inefficient or inaccessible at the test stage, thus, we adopt the loss terms in Eq (35), *i.e.*, $\ell_{fid}^{(i)}$, $\ell_{rank}^{(i)}$ and $\ell_{sparse}^{(i)}$, calculated solely on \mathcal{D}_{ood} for $\hat{\mathcal{L}}_{\text{AG}}$. In addition, one can solely fine-tune selected module(s), such as the sparse module (f_{θ_s}) for sparsity-sensitive applications, while keeping other modules frozen, thanks to the modularized architecture of f_θ and the separability of the loss function. For such commonly seen scenario, we have the loss function,

$$\hat{\mathcal{L}}_{\text{AG}} := \hat{\mathcal{L}}_{\text{AG}_s} = \frac{1}{|\mathcal{D}_{ood}|} \sum_{i=1}^{|\mathcal{D}_{ood}|} (\ell_{fid}^{(i)} + \ell_{sparse}^{(i)}). \quad (39)$$

Similarly, there is a less common scenario when one needs only adaptation on the low-rank module. The loss becomes,

$$\hat{\mathcal{L}}_{\text{AG}} := \hat{\mathcal{L}}_{\text{AG}_L} = \frac{1}{|\mathcal{D}_{ood}|} \sum_{i=1}^{|\mathcal{D}_{ood}|} (\ell_{fid}^{(i)} + \ell_{rank}^{(i)}). \quad (40)$$

Finally, one may perform the adaptation on both of the two modules, resulting in a loss, as follows,

$$\hat{\mathcal{L}}_{\text{AG}} := \hat{\mathcal{L}}_{\text{AG}_{LS}} = \frac{1}{|\mathcal{D}_{ood}|} \sum_{i=1}^{|\mathcal{D}_{ood}|} (\ell_{fid}^{(i)} + \ell_{rank}^{(i)} + \ell_{sparse}^{(i)}). \quad (41)$$

Note that simultaneously fine-tuning these two modules can be challenging due to their entanglement. Section 4.4 provides more discussion.

Online active generalization: Given an OOD image during the test phase, InDeedOAG executes two sequential operations on the image, *i.e.*, model adaptation through active generalization followed by inference. InDeedOAG presents high efficiency and effectiveness, as Section 4.4 will demonstrate.

To prevent model collapse and large fluctuations in K , we apply early-stopping [71]. Algorithms in Section 3 of Supplementary Material provide pseudocodes.

3.6 Applications

We exemplify InDeed using two downstream tasks, namely, image denoising (DEN) and unsupervised anomaly detection (UAD), with specific supervision loss ℓ_{sup} . Furthermore, to ensure the two low-rank components capture diverse information, we apply an additional orthogonal constraint,

$$\ell_{orth} = \|\hat{A}^T \hat{A} - I\|_F^2 + \|\hat{B}^T \hat{B} - I\|_F^2, \quad (42)$$

where \hat{A} and \hat{B} are respectively the sampled left and right factors of low-rank components. The overall loss function becomes,

$$\hat{\mathcal{L}}_{\text{DEN/UAD}} = \hat{\mathcal{L}}_{\text{dnn}} + \tau \sum_{i=1}^{|\mathcal{D}_{tr}|} \ell_{orth}^{(i)}, \quad (43)$$

where τ is a balancing weight. In the following, we specify the supervision loss ℓ_{sup} in Eq. (35) for the two tasks.

For image denoising, we consider the target ($U \in \mathbb{R}^{h \times w}$) to be the clean image of the observation. For convenience, we use the low-rank variable L instead of A and B for illustration. Specifically, given $\mathcal{Z}_m = \{L, S\}$, the likelihood w.r.t. U can be modeled as i.i.d Gaussian distributions with a hyper-parameter σ_0 , namely, $p(U|\mathcal{Z}_m) = \prod_{i=1}^{h,w} \mathcal{N}(u_{ij}|l_{ij} + s_{ij}, \sigma_0^{-1})$. Hence, by adopting the same reparameterization technique in Eq. (32), the supervision loss ℓ_{sup} can be intuitively expressed as, $\ell_{sup} = -\mathbb{E}_{q(\mathcal{Z}_m)}[\log p(U|\mathcal{Z}_m)] \approx \frac{\sigma_0}{2} \|\hat{L} + \hat{S} - U\|_F^2$. However, minimizing this term could result in a naive solution of $\hat{L} = 0$ and $\hat{S} = U$, which deviates from our assumption that \hat{L} is a low-rank approximation of U . Therefore, we propose to include an additional loss of $\|\hat{L} - U\|_F^2$ to avoid such problem, namely,

$$\ell_{sup|\text{DEN}} = \frac{\sigma_0}{2} (\|\hat{L} + \hat{S} - U\|_F^2 + \|\hat{L} - U\|_F^2). \quad (44)$$

For unsupervised anomaly detection, we generate abnormal samples Y from normal observations $U_N \in \mathbb{R}^{h \times w}$ and synthetic anomalies $U_A \in \mathbb{R}^{h \times w}$, by a self-supervised scheme (Please refer to Section 4.3 of Supplementary Material). Specifically, U_A is expressed as $U_A = Y - U_N$ to satisfy the decomposition. Thereby, we have the ground truth $U = \{U_N, U_A\}$, and $p(U_A, U_N|\mathcal{Z}_m) = p(U_A|S)p(U_N|L)$. We model U_A as i.i.d Gaussian distributions with a user-determined hyper-parameter σ_0 , namely, $p(U_A|S) = \prod_{i=1}^{h,w} \mathcal{N}(U_{a_{ij}}|s_{ij}, \sigma_0^{-1})$. Similarly, we define $p(U_N|L) = \prod_{i=1}^{h,w} \mathcal{N}(U_{n_{ij}}|l_{ij}, \sigma_0^{-1})$. Hence, the supervision loss for UAD is given by,

$$\ell_{sup|\text{UAD}} = \frac{\sigma_0}{2} (\|\hat{L} - U_N\|_F^2 + \|\hat{S} - U_A\|_F^2). \quad (45)$$

4 EXPERIMENTS

In this section, we first introduced data and implementation details in Section 4.1 and performed ablation studies in Section 4.2. Then, we evaluated the performance of InDeed on two tasks, *i.e.*, image denoising and unsupervised anomaly

detection (UAD) in Section 4.3.1 and 4.3.2, respectively. Subsequently, in Section 4.4 we further studied the performance of active generalization in out-of-distribution scenarios. Finally, in Section 4.5 we discussed the interpretability of each module and analyzed their contribution to model performance. *For more results and visualization, please refer to Section 5 in Supplementary Material.*

4.1 Data and implementation details

For image denoising, we utilized the DIV2K dataset [72] for model training and ablation studies, consisting of 800 training and 100 validation high-resolution images. Gaussian white noise (AGWN) with noise levels ranging between $[0, 75]$ was added to generate noisy images. For in-distribution denoising evaluation, we used three widely-used high-quality datasets: CBSD68 [73], Kodak24 [74], and McMaster [75]. To assess generalizability, we employed two real-world noisy datasets: SIDD (small version) [40] with 160 images from 10 scenes using five smartphone cameras, and PolyU [76], containing 100 images from 40 scenes using five cameras. Two metrics were used to evaluate the performance, *i.e.*, the standard Peak Signal to Noise Ratio (PSNR) and the Structural Similarity (SSIM) index.

For unsupervised anomaly detection, we used MVTecAD [77] for training and in-distribution evaluation. MVTecAD includes 15 object classes with 3629 training and 1725 test images. Each class is further divided based on the type of anomaly, resulting in a total of 73 defect subclasses (excluding the "good" subclass). To assess generalizability, we used three OOD datasets: noisy MVTecAD, Severstal steel images [78], and the Medical OOD (MOOD) dataset [79]. Noisy MVTecAD was generated by adding AGWN ($\sigma = 2.55$) to MVTecAD test images. The Severstal dataset is a steel defect detection dataset, and we randomly selected 256 images for evaluation. Finally, the MOOD dataset is for OOD medical image analysis. We evaluated the models on its validation set with 5 brain MRI toy cases. We adopt two commonly used metrics [44] to evaluate the performance, *i.e.*, the average precision (AP), and the area under ROC curve (AUROC) scores. *Note that when the positive and negative data are severely imbalanced, the AUROC metric may be inflated [80], while the AP score, which summarizes the precision-recall (PR) curve, can indicate the level of false positives.*

In the training stage, we set the image size $h \times w$ as 128×128 . For the hyper-parameters, we set $\alpha_\gamma^0 = \alpha_\omega^0 = \alpha_\lambda^0 = 2$, $\beta_\gamma^0 = \beta_\omega^0 = 1 \times e^{-6}$ and $\beta_\lambda^0 = 1 \times e^{-8}$ in Eq. (19), (21) and (22), $r^0 = 64$ in Eq. (16), and the balancing parameters $\tau = 1$ in Eq. (43). We trained our models using the ADAM [81] optimizer for 2000 epochs. The initial learning rate was 1×10^{-4} , and decayed by a factor of 0.5 every 200 epochs. During testing, we divided each image into overlapping 128×128 patches if not divisible by 128, and stitched the results to form the final prediction at the original size. The proposed method was implemented via Pytorch, and all models were trained and tested on an RTX 3090 GPU with 24 GB memory.

4.2 Ablation study

We employed the image denoising task and DIV2K dataset for this study. The training set and the validation set at the noise level of $\sigma = 25$ were respectively used for our models.

TABLE 3: Ablation Study of InDeed with different backbones, depth-kernel pairs (d, ks), maximal rank r^0 , normalization strategies, and loss functions. The results of L present metrics calculated via L and U , indicating low-rank estimation quality. $L + S$ refers to the recovery image, with its results as denoising performance. *BatchNorm*: *Batch Normalization*; *GroupNorm*: *Group Normalization*. Bold fonts indicate the best results.

Model	Settings					L		$L + S$		#Para
	Backbone	(d, ks)	r^0	Norm	loss function	PSNR \uparrow	SSIM \uparrow	PSNR \uparrow	SSIM \uparrow	
#1	ResNet	(15, 7)	64	GroupNorm	$\hat{\mathcal{L}}_{\text{DEN}}$ in Eq. (43)	22.27	0.6335	31.69	0.9217	8.8M
#2		(21, 5)				22.67	0.6612	28.54	0.8744	7.5M
#3		(35, 3)				22.69	0.6618	32.32	0.9278	5.8M
#4	ResNet	(35, 3)	4	GroupNorm	$\hat{\mathcal{L}}_{\text{DEN}}$ in Eq. (43)	17.08	0.4803	31.59	0.8768	5.8M
#5			8			18.38	0.5065	31.58	0.8769	5.8M
#6			16			19.50	0.5088	31.70	0.8786	5.8M
#7			32			21.12	0.5610	31.71	0.8790	5.8M
#8			96			20.96	0.5625	31.58	0.8792	5.8M
#9	ResNet	(35, 3)	64	GroupNorm	$\hat{\mathcal{L}}_{\text{DEN}}$ w/o $\ell_{\text{rank}}, \ell_{\text{sparse}}, \ell_{\text{fid}}$	13.01	0.5180	32.16	0.8891	5.8M
#10	ResNet	(35, 3)	64	BatchNorm	$\hat{\mathcal{L}}_{\text{DEN}}$ in Eq. (43)	12.18	0.4030	31.91	0.8819	5.8M
#11	Transformer	N/A	64	N/A	$\hat{\mathcal{L}}_{\text{DEN}}$ in Eq. (43)	21.00	0.5570	30.87	0.8713	79M

TABLE 4: In-distribution study of color image denoising with different noise level (σ). Bold fonts indicate the best results and the italics indicate the second-best result.

Dataset	Method	$\sigma = 15$		$\sigma = 25$		$\sigma = 35$		$\sigma = 50$	
		PSNR	SSIM	PSNR	SSIM	PSNR	SSIM	PSNR	SSIM
CBSD68	CBM3D [82]	33.52	.9248	30.71	.8716	28.89	.8207	27.38	.7669
	CDnCNN [83]	33.89	.9317	31.23	.8863	29.58	.8452	27.92	.7915
	FFDNet [84]	33.87	.9318	31.21	.8857	29.58	.8445	27.96	.7916
	RONet-C [85]	33.99	.9336	31.36	.8902	29.74	.8514	28.14	.8009
	VIRNet [86]	34.27	.9340	31.65	.8918	30.04	.8548	28.45	.8083
	InDeed	<i>34.06</i>	<i>.9329</i>	31.67	.8990	29.98	.8483	<i>28.15</i>	<i>.8020</i>
Kodak24	CBM3D [82]	34.28	.9164	31.68	.8682	29.90	.8212	28.46	.7751
	CDnCNN [83]	34.48	.9212	32.03	.8774	30.46	.8390	28.85	.7895
	FFDNet [84]	34.64	.9230	32.13	.8790	30.57	.8407	28.98	.7929
	RONet-C [85]	34.80	.9234	32.33	.8845	30.77	.8484	29.18	.8020
	VIRNet [86]	35.15	.9283	32.75	.8908	31.22	.8583	29.69	.8186
	InDeed	35.15	.9259	32.66	.9000	<i>31.16</i>	<i>.8436</i>	<i>29.43</i>	<i>.8095</i>
McMaster	CBM3D [82]	34.06	.9150	31.66	.8739	29.92	.8327	28.51	.7934
	CDnCNN [83]	33.44	.9070	31.51	.8724	30.14	.8412	28.61	.7985
	FFDNet [84]	34.66	.9247	32.35	.8891	30.81	.8573	29.18	.8157
	RONet-C [85]	34.77	.9251	32.51	.8920	31.00	.8627	29.39	.8245
	VIRNet [86]	35.32	.9312	33.08	.9016	31.59	.8758	30.02	.8434
	InDeed	<i>35.07</i>	<i>.9256</i>	33.52	.8926	31.22	.8438	29.50	.8345

We first investigated the impact of model depth d and kernel size ks for f_{θ_L} , adjusting them jointly to maintain the full receptive field. Three configurations of (d, ks) were explored, and Models #1-3 were trained accordingly. Model #3 achieved the best performance at $(d, ks) = (3, 35)$. Next, we examined the effect of the maximum rank r^0 . As r^0 increased, the performance of L and $L + S$ peaked at $r^0 = 64$, which is close to the average rank of clean images in DIV2K, estimated as 73 via SVD. The performance of L was more sensitive to changes in r^0 , as its representation is limited by r^0 , while $L + S$ can be compensated by f_{θ_S} .

To study the impact of loss functions, we trained Model #9 by minimizing $\hat{\mathcal{L}}_{\text{DEN}}$ without $\ell_{\text{rank}}, \ell_{\text{sparse}}$ and ℓ_{fid} . While its performance on $L + S$ was comparable to Model #3, the L component deviated from the optimal low-rank representation, leading to a less interpretable end-to-end network. To evaluate the utility of GroupNorm, Model #10 was trained with BatchNorm instead. The results indicated that GroupNorm was essential for capturing an optimal low-rank representation, since BatchNorm, applying normalization over a mini-batch, was less suited for the independent modeling of column vectors in A and B in Eq. (17) and (18). GroupNorm, normalizing channel-wise, was then proved more appropriate here. Finally, we replaced the backbone with a transformer in Model #11, which nevertheless led to an evident performance drop.

Based on the above study, we adopted the setting of Model #3 for the following studies unless stated otherwise.

4.3 General performance

4.3.1 Image denoising

In this section, we studied the performance of InDeed on both Gaussian denoising and real-world denoising tasks. We trained InDeed with noisy DIV2K images, with the noise level σ of AGWN uniformly distributed in $(0, 75]$.

In-distribution performance of Gaussian denoising.

We evaluated InDeed on CBSD68, Kodak24, and McMaster at different noise levels ($\sigma \in \{15, 25, 35, 50\}$) and compared it with five SOTA methods: BM3D [82], DnCNN [83], FFDNet [84], RONet-C [30], and VIRNet [86].

Table 4 shows the results. One can see that the best performance in each task was achieved by either InDeed or VIRNet. One particular phenomenon occurs at $\sigma = 25$, where InDeed outperforms VIRNet in four out of six metrics. Fig. 3 provides three typical examples from our study, showing the visual difference of the denoised results by the compared methods. Furthermore, we implemented InDeed for gray-scale Gaussian denoising, which demonstrated a comparable performance, achieving the best scores in 16 metrics (out of 24). *Please refer to Section 5.1 in Supplementary Material for more details.*

OOD generalizability in real-world denoising. We evaluated InDeed on SIDD and PolyU datasets without retraining, and compared with RONet-C [30], VIRNet [86], and MaskedDen [43], which were particularly developed for OOD generalization. Table 5 (A) presents the results. InDeed performed better than RONet and VIRNet in 23 out of 24 metrics (only in C2 of PolyU, VIRNet had a better PSNR score). This indicates the superior generalizability of explicit modeling of image decomposition. Note that MaskedDen achieved the best results in the SIDD dataset, which could not be considered as an OOD scenario, and it experienced a significant performance drop in PolyU when it was OOD. This is because MaskedDen was trained with the setting of Gaussian noise level as $\sigma = 15$, which was close to the noise level of SIDD (thus considered as in-distribution).

4.3.2 Unsupervised anomaly detection

We first trained one single model with all classes from MVTEC-AD, following uniAD [47], and then compared it

TABLE 5: Generalizability of image denoising on two out-of-distribution datasets, *i.e.*, SIDD and PolyU. ADP refers to the adaptation time. Bold font indicates the best result within each subtable, and an underline denotes the best result across the entire table.

Method	Metric	SIDD						PolyU							
		G4	GP	IP	N6	S6	mean	ADP	C1	C2	C3	C4	C5	mean	ADP
(A) OOD performance without active generalization															
MaskedDen $_{[\sigma=15]}$ [43]	PSNR	34.79*	33.21*	34.86*	29.60*	29.25*	32.56*	-	32.69	34.15	35.05	34.98	32.50	33.80	-
	SSIM	.8777*	.8160*	.8680*	.6307*	.6650*	.7812*	-	.9561	.9675	.9288	.9366	.9138	.9387	-
RONet-C [85]	PSNR	30.16	29.83	29.40	26.30	25.87	28.36	-	31.74	35.00	34.17	34.19	32.42	33.22	-
	SSIM	.6281	.6203	.5702	.4499	.4621	.5461	-	.9291	.9232	.9380	.9246	.8868	.9198	-
VIRNet [86]	PSNR	29.64	29.64	28.91	25.92	25.70	28.02	-	34.09	36.89	36.73	35.95	32.80	34.98	-
	SSIM	.6179	.6160	.5594	.4397	.4512	.5368	-	.8865	.9146	.9180	.9164	.8400	.8930	-
InDeed	PSNR	31.42	30.88	30.94	27.29	27.24	29.68	-	34.67	36.47	36.74	36.06	33.47	35.26	-
	SSIM	.6878	.6564	.6551	.4921	.5115	.6054	-	.9363	.9326	.9244	.9219	.8920	.9210	-
(B) OOD Performance with active generalization (AG)															
InDeedAG	PSNR	34.39	33.11	34.02	29.65	29.55	32.29	28s	35.94	38.75	38.34	37.24	35.30	36.75	20s
	SSIM	.8084	.7488	.8016	.5914	.6103	.7206	-	.9613	.9567	.9547	.9544	.9324	.9521	-
InDeedAG $_{\beta}$ (L)	PSNR	31.13	30.20	31.06	27.49	27.67	29.67	21s	35.27	37.27	37.37	36.73	34.14	35.93	17s
	SSIM	.7584	.6808	.7156	.5572	.5733	.6598	-	.9396	.9314	.9371	.9365	.9014	.9300	-
InDeedAG $_{\beta}$ (LS)	PSNR	31.83	31.14	31.17	27.56	27.54	29.94	22s	35.31	37.46	37.32	36.63	34.18	35.92	13s
	SSIM	.7032	.6656	.6644	.5009	.5220	.6149	-	.9437	.9390	.9387	.9409	.9045	.9340	-
(C) OOD Performance with online active generalization (OAG)															
InDeedOAG	PSNR	35.94	34.63	36.03	32.95	32.24	34.48	0.07s/ image	35.67	38.66	38.48	37.49	35.68	36.84	0.04s/ image
	SSIM	.9043	.8622	.8913	.8061	.7931	.8534	-	.9520	.9573	.9554	.9550	.9414	.9517	-

*MaskedDen $_{[\sigma=15]}$ was trained with Gaussian noise at $\sigma = 15$, similar to that of SIDD. Hence, these results in (A) are not considered as OOD.

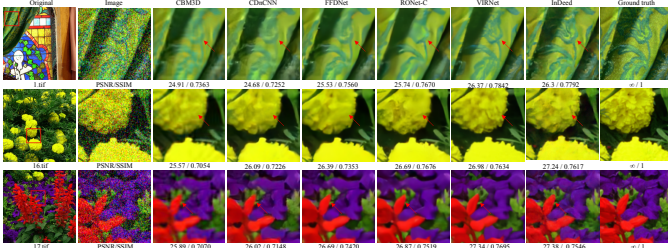


Fig. 3: Visualization of color image denoising under $\sigma = 50$. Three typical examples (cropped patches of size 100×100 , denoted by red boxes) from McMaster. Please zoom in the online electronic version for more details.

with six state-of-the-art (SOTA) methods, including uniAD [47], DRAEM [44], FAVAE [51], FastFlow [53], CutPaste [55], and STPM [87] in both in-distribution and OOD scenarios. We utilized the official model of UniAD and retrained the other five SOTA models under the same setting. Specifically, we clustered the 73 defect classes into three groups, namely, Low, Mid, and High, according to the rank of test images estimated by SVD, to better present the inherent variability of UAD in terms of image rank.

In-distribution performance. Table 6 presents results on the MVTEcAD test dataset. One can see InDeed and uniAD ranked the top two in all categories. When solely comparing these two methods, one can conclude that uniAD tended to produce more false-positive predictions, as it obtained marginally better AUROC (*e.g.*, Mid: 94.8% vs. 94.6%) but evidently lower AP values (*e.g.*, Mid: 66.1% vs. 74.8%), compared to InDeed.

Fig. 4 visualizes the results of six samples selected from the three groups by all the compared methods. Both InDeed and uniAD performed well in these cases, though uniAD could generate more false positives. This is consistent with the previous conclusion from Table 6. One may also find that InDeed could be challenged in distinguishing these normal pixels exhibiting sparsity property from anomalies,

TABLE 6: In-distribution study of unsupervised anomaly detection on MVTEcAD dataset. Bold font indicates the best result, and italics indicate the second-best result.

Method	AP (%) \uparrow			AUROC (%) \uparrow		
	Low	Mid	High	Low	Mid	High
FastFlow [53]	0.41	22.5	5.15	68.4	67.5	61.2
CutPaste [55]	0.56	22.5	6.37	65.5	66.6	63.6
DRAEM [44]	0.23	30.4	21.8	11.4	50.4	62.6
FAVAE [51]	0.48	36.4	11.9	55.4	80.8	61.2
STPM [87]	7.40	35.8	15.4	75.0	86.4	71.5
uniAD [47]	39.7	66.1	47.1	99.1	94.8	95.8
InDeed	46.7	74.8	51.8	99.5	94.6	90.0

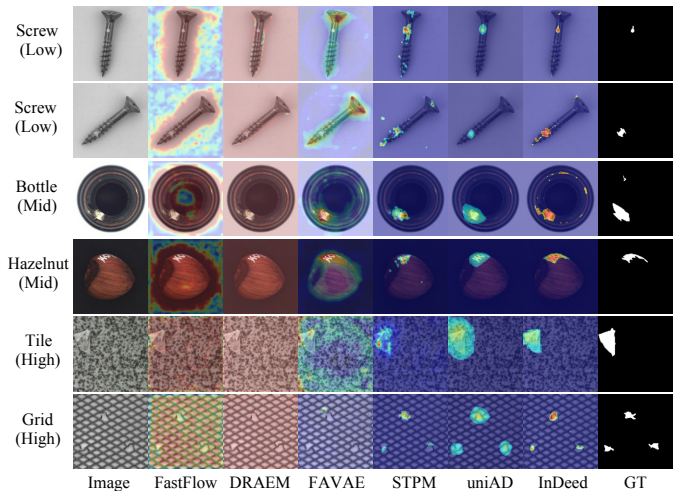


Fig. 4: Examples from MVTEcAD and the anomaly map overlay. Note that the color of original images may look different when they are overlaid with the anomaly maps, due to the mixture of colors. GT: ground truth segmentation map.

such as the hot spots on sample "Bottle", which could lead to misclassification.

OOD performance. We further evaluated the generalizability with three OOD datasets, *i.e.*, noisy MVTEcAD, Severstal, and MOOD. Note that for the noisy MVTEcAD,

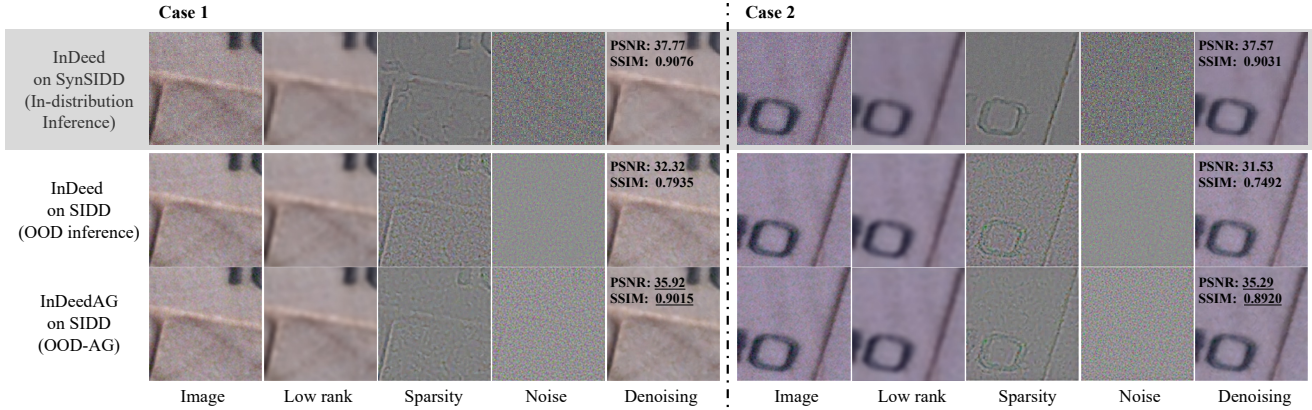


Fig. 5: Visual comparisons between InDeed and InDeedAG on two cases from SIDD (cropped patches of size 100×100). Note that “InDeed on SynSIDD” serves as reference, representing predictions using synthetic in-distribution images with AWGN ($\sigma = 15$). One can see that InDeedAG achieves better decomposition results than InDeed, particularly evident in noise components, leading to better PSNR and SSIM.

TABLE 7: Generalizability in terms of unsupervised anomaly detection. Symbol Δ refers to the decrease compared with the performance on the clean image.

	Noisy MVtecAD (Mid)		Severstal		MOOD	
	AUROC \uparrow ($\Delta \downarrow$)	AP \uparrow ($\Delta \downarrow$)	AUROC \uparrow	AP \uparrow	AUROC \uparrow	AP \uparrow
DRAEM	N/A	N/A	40.1	5.56	N/A	N/A
FastFlow	N/A	N/A	55.5	10.7	N/A	N/A
FAVAE	N/A	N/A	83.3	32.1	N/A	N/A
STPM	69.4 (17.0)	28.2 (27.4)	85.8	37.0	73.4	1.61
uniAD	73.0 (21.8)	10.5 (55.6)	90.4	38.9	80.6	1.67
InDeed	90.4 (4.22)	69.1 (5.74)	87.8	46.2	82.4	44.3

the performance of each method was reported in group Mid. The completed results and visualizations are presented in Section 5.2 of Supplementary Material.

Table 7 provides the results. Overall, only STPM, uniAD, and InDeed produced reasonable results across all datasets, whereas the other three methods failed on both Noisy MVtecAD and MOOD. For Noisy MVtecAD, InDeed achieved the best AP (69.1%) and AUROC (90.4%) scores, demonstrating robustness with only a slight decrease of 5.74% in AP and 4.22% in AUROC, compared to the noise-free scenario. For the Severstal and MOOD datasets, InDeed and uniAD achieved comparable AUROC, but similar to the in-distribution scenario, uniAD had evidently lower AP scores.

4.4 Studies of OOD active generalization

To study the effectiveness of OOD active generalization (AG), namely InDeedAG, we adaptively finetuned the pre-trained InDeed model with OOD test data. During finetuning, the learning rate η and batch size were set as 1×10^{-6} and 1, respectively.

4.4.1 Image Denoising

We used the SIDD and PolyU datasets for real-world image denoising study. Four variants of active generalization were studied: (1) InDeedAG: solely adapt the sparsity module using Eq. (39), (2) InDeedAG β (L): solely adapt the low-rank module using Eq. (40), (3) InDeedAG β (LS): adapt the two modules simultaneously using Eq. (41), (4) InDeedOAG: online active generalization with adaptation solely on the sparsity module for each test image.

Results. Table 5 presents the results. InDeedAG outperformed all the OOD tested models without active generalization in Table 5 (A). Particularly, active generalization boosted performance of InDeed on SIDD by 2.61 dB in PSNR and 0.1152 in SSIM, and on PolyU by 1.49 dB in PSNR and 0.0311 in SSIM. Notably, the adaptation times (ADP) on the two datasets were only 28s and 20s, respectively, highlighting the efficiency of InDeedAG. In addition, InDeedOAG further improved the performance of InDeedAG on SIDD with an increase of 2.19 dB in PSNR and 0.1328 in SSIM, though the improvement on PolyU was not evident. Again, InDeedOAG was also efficient, with 0.04-0.07 second expense per image for online active generalization.

Comparing the results solely in Table 5 (B), InDeedAG, with adaptation solely on the sparsity module (f_{θ_S}), performed evidently better than InDeedAG β (L), demonstrating that adapting f_{θ_S} is more effective in handling noise shifts. This is because f_{θ_S} is designed to capture sparse image details from noisy data, making it more sensitive to OOD noise. In contrast, the low-rank module (f_{θ_L}) captures low-rank information, which nevertheless focuses on global consistency and thus is inherently robust to perturbations like noise shift. In addition, one can see that InDeedAG β (LS) did not show significant improvement on either dataset and even sometimes performed worse than InDeedAG β (L). This suggests that simultaneously adapting multiple modules can pose additional challenges to the framework.

Visualization for interpretation. Fig. 5 shows the image decomposition results on two samples from the SIDD dataset. Here, *OOD inference* and *OOD-AG* refer to results predicted by InDeed without active generalization and InDeedAG, respectively. For reference, we also present the results of *In-distribution inference*, in which InDeed was applied to synthetic noisy images, referred to as SynSIDD, created by adding AWGN with $\sigma = 15$ to the ground truth images. One can see that the predicted sparsity components (S) from OOD inference were more intertwined with noise, resulting in much lower values of PSNR and SSIM. However, after active generalization the sparsity and noise components were decomposed more separately by InDeedAG, leading to improved PSNR and SSIM on both cases.

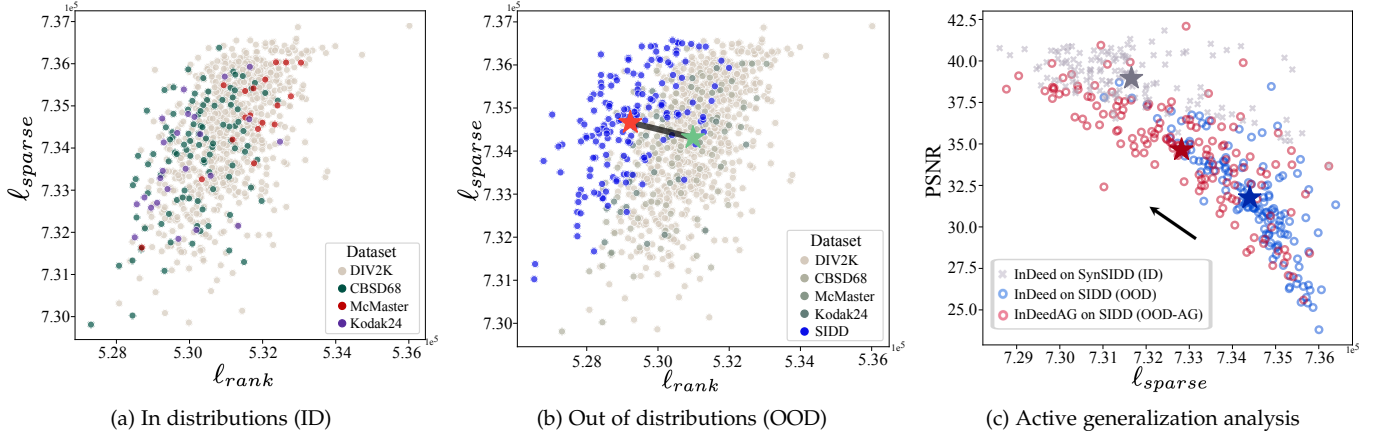


Fig. 6: Impacts of l_{rank} and l_{sparse} on identifying OOD datasets (in (a-b)) and facilitating active generalization (in (c)). (a) and (b): Joint distributions of (l_{rank}, l_{sparse}) for in-distribution (ID) and OOD test datasets, respectively. Gray points represent training samples from DIV2K. In (b), one can see that SIDD shows OOD behavior, with its average point (red star) deviating from DIV2K’s (green star). (c): Joint distributions of $(l_{sparse}, PSNR)$ for InDeed and InDeedAG. InDeed on SynSIDD represents ID inference. InDeed on SIDD shows higher l_{sparse} and lower PSNR, whereas InDeedAG reduces loss and boosts performance. The arrow illustrates the trend from InDeed’s mean point to InDeedAG’s.

Interpretation in terms of loss functions. We further elaborate on the effect of active generalization from the aspect of loss terms, *i.e.*, l_{sparse} and l_{rank} in Eq. (35).

Firstly, to study the effect of such pair (l_{sparse}, l_{rank}) in indicating the severity of OOD, we calculated them for each image from different datasets, and visualized their distributions. In Fig. 6 (a), sample points of CBSD68, McMaster, and Kodak24 with AGWN ($\sigma = 15$), are distributed inside the distribution of the training dataset, *i.e.*, DIV2K, confirming in-distribution (ID). In contrast, Fig. 6 (b) shows that sample points from SIDD, an OOD dataset compared to DIV2K, exhibit a distribution of lower level of l_{rank} and larger l_{sparse} . One can notice the disparity from the distinct deviation of its average point (red star) from DIV2K’s (green star). These observations are consistent with our experimental design, illustrating the shift from Gaussian noise to real-world noise, suggesting the pair of loss terms serve as effective metrics for assessing distribution discrepancy.

Secondly, we study the effect of OOD active generalization. Note that the increased l_{sparse} in OOD datasets can be a main source impeding model generalizability. Hence, the adaptation of f_{θ_S} could be effective. Fig. 6 (c) visualizes the distribution of the value pair $(l_{sparse}, PSNR)$, predicted by InDeed and InDeedAG with adaptation on the sparsity module. Fig. 6 (c) also presents the distribution of InDeed on in-distribution (ID) SynSIDD as reference. Compared with the synthetic ID reference, InDeed on SIDD (OOD) demonstrated relatively higher l_{sparse} and lower PSNR values. In contrast, after fine-tuning f_{θ_S} , InDeedAG reduced l_{sparse} significantly, resulting in higher PSNR values.

4.4.2 Unsupervised anomaly detection

For this study, we adapted f_{θ_S} of InDeed to the noisy MVTECAD dataset via active generalization (InDeedAG) and online active generalization (InDeedOAG), for comparisons.

InDeedAG achieved AP and AUROC scores of 69.5 and 90.5, respectively, surpassing InDeed by 0.04 in AP and

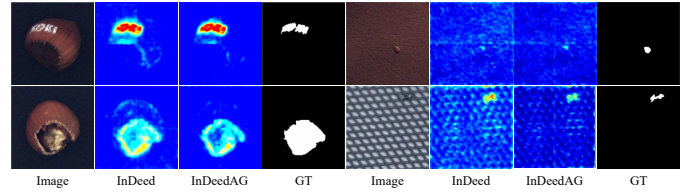


Fig. 7: Visual comparisons between InDeed and InDeedAG: the latter can further removes the false positives in UAD. The color map images are the anomaly maps. GT: ground truth segmentation map.

0.01 in AUROC; and InDeedOAG surpassed InDeed by 0.01 in AP and 0.02 in AUROC. One can read that the performance gains in terms of AP and AUROC for both of the two active generalization methods were limited. We therefore further investigated the anomaly maps predicted by these methods. Fig. 7 visualizes four typical cases from InDeed and InDeedAG. One can see that the predictions of InDeed were more crippled by noise, with blurry delineation of defects and false-positive patterns. In contrast, InDeedAG alleviated the noise effect, resulting in clearer defect boundaries and fewer false-positive pixels in the background. This visual investigation indicated that active generalization could further remove false positives, though the quantitative metrics may not be able to capture this performance gain.

4.5 Interpretability study

In this section, we investigated the interpretability of InDeed from two aspects, (1) the representation of intermediate outputs and (2) the interpretation of the low rank and sparsity terms, *i.e.*, l_{rank} and l_{sparse} in Eq. (35).

4.5.1 Visualization of intermediate outputs

To demonstrate the interpretability of each module, we visualized the outputs of InDeed, namely posteriors of variables

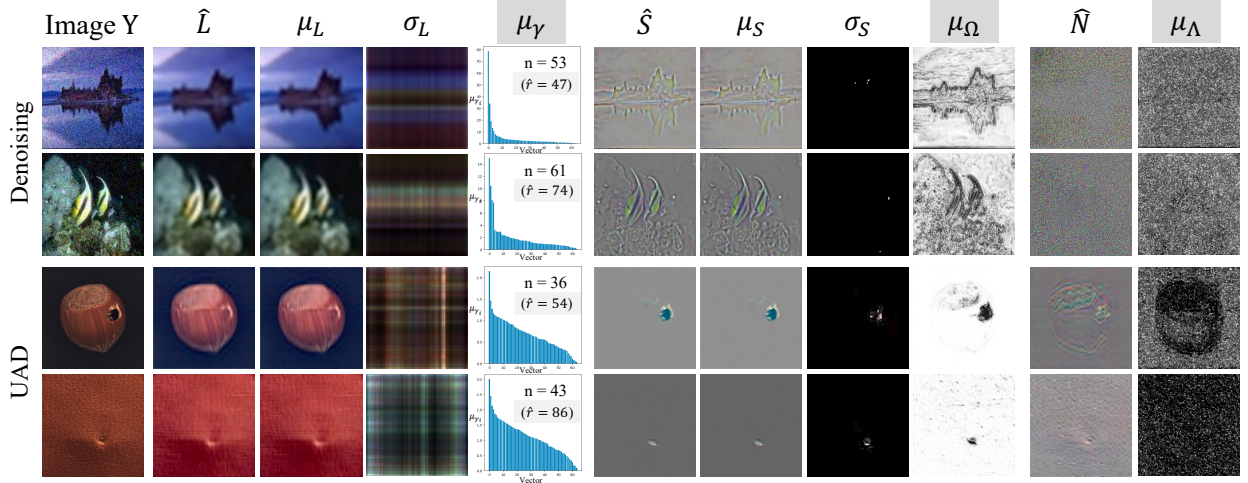


Fig. 8: Visualization of posteriors inferred by InDeed for two tasks. For middle-level variables, the sampled result ($\hat{L}/\hat{S}/\hat{N}$), mean ($\mu_{L/S}$), and standard deviation ($\sigma_{L/S}$) are shown. For leaf-level variables, expectations ($\mu_{\gamma/\Omega/\Lambda}$) are displayed. Note that for $\sigma_{L/S}$ and $\mu_{\Omega/\Lambda}$, we display the logarithmic values, (e.g., $\log(\sigma_L)$) for better visual effects. For $\mu_{\gamma} \in \mathbb{R}^{r^0}$, we show the histogram for each image, along with the image rank \hat{r} computed via SVD and the proposed index n for reference. For $\mu_{\Omega/\Lambda}$, we calculated the norm pixel-wisely, with brighter pixels indicating a higher possibility of being zero in corresponding samples.

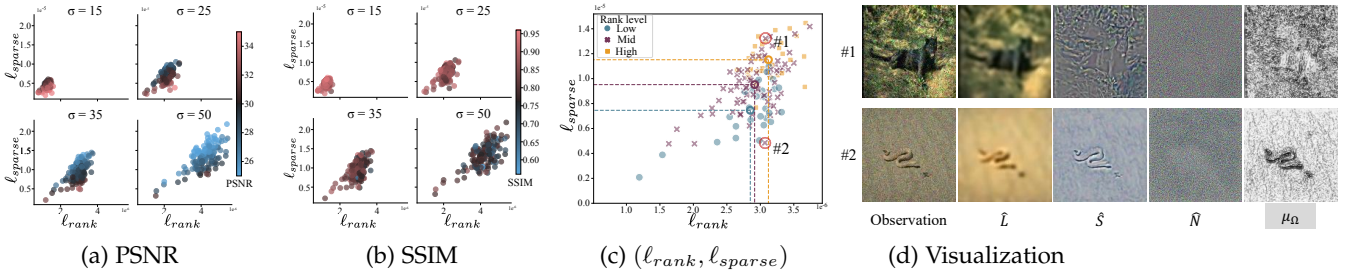


Fig. 9: Relationship between $(\ell_{rank}, \ell_{sparse})$ and denoising performance (in (a-b)) and image details (in (c-d)). (a) and (b) show the correlation with performance, quantified by (a) PSNR and (b) SSIM, under different noise levels. Each point refers to an ID test image. (c) looks at the effect on image detail. Images are categorized by their ranks determined via SVD. One can see that the image with a higher rank tends to have a higher ℓ_{rank} . Furthermore, despite similar ℓ_{rank} levels, as demonstrated in Case #1 and #2, ℓ_{sparse} can differ. (d) compares the decomposition results for Cases #1 and #2, illustrating that their S present distinct levels in terms of the richness of details, controlled by μ_{Ω} with higher values.

$\mathcal{Z} = \{L, S, N, \gamma, \Omega, \Lambda\}$, as Fig. 8 shows. Note that for L , its mean and variance can be explicitly computed from those of A and B , i.e., $\mu_L = \frac{\mu_A(\sigma_B^T)^2 + \sigma_A^2 \mu_B^T}{\sigma_A^2 I_B^T + I_A(\sigma_B^T)^2}$ and $\sigma_L^2 = \frac{\sigma_A^2(\sigma_B^T)^2}{\sigma_A^2 I_B^T + I_A(\sigma_B^T)^2}$. Moreover, for reference we introduced an index based on γ , defined as $n = |I|$, where $I = \{i | p(\gamma_i^{-1}) > threshold\} > 0.95\}$.

For the low-rank components, we visualized a sample \hat{L} , its mean μ_L , standard deviation σ_L , and the expectation of leaf-level variable γ , namely μ_{γ} . One can see that L captures the structure information (dominant features) of an image, in both denoising and UAD, which is consistent with our modeling. Note that for UAD, L approximates the low-rank representation of normal images rather than those with anomalies, which is guided by the modeling of target U formulated in Eq. (45). Moreover, the histograms of μ_{γ} shows the capability of rank adaptation for each case. The indicator of estimated rank n is close to \hat{r} for image denoising in the two cases. In the second case where $\hat{r} = 74$, n is close to the maximum value $r^0 = 64$, which is the upper

limit of our rank modeling. In the two cases of UAD, there is a significant gap between n and \hat{r} . This is desirable, because L models the normal low-rank pattern, whereas \hat{r} calculates the rank from the original images that contained anomalies, resulting in the inherent deviation. Although InDeed shows rank adaptability, accurately determining the rank of low-rank estimation remains a challenge.

For the sparsity components, we visualized a sample \hat{S} , mean μ_S , standard deviation σ_S , and mean value of the sparsity-controlling variable Ω , namely μ_{Ω} . Note that \hat{S} represents task-specific sparsity information, guided by the distinct supervision losses, i.e., $\ell_{sup|DEN}$ and $\ell_{sup|UAD}$ in Eq. (44) and Eq. (45). For denoising, S captured structural information such as boundaries, while for UAD, it extracts patterns distinct from normal regions and without high self-consistency, such as anomalies. Moreover, the figures for μ_{Ω} demonstrate high consistency with the sparsity modeling. For example, the high values of μ_{Ω} in the background of the images mean a high possibility of sparsity in these areas,

which is consistent with the presentation in \hat{S} .

For the noise components, N exhibits different representations for each task. For image denoising, N captures the pixel-wise Gaussian noise, while for UAD, it represents the residual texture information.

4.5.2 Interpretation of loss function

We interpreted the low-rank and sparsity terms, namely, l_{rank} and l_{sparse} from two aspects, taking the image denoising as an example.

Firstly, we analyzed the relationship between pair (l_{rank}, l_{sparse}) and performance. In the in-distribution study of image denoising in Section 4.3.1, we calculated triplets $(l_{rank}, l_{sparse}, \text{PSNR/SSIM})$ for all images with noise levels $\sigma \in \{15, 25, 35, 50\}$ using the trained model, and illustrated their distributions in Fig. 9 (a) and (b), respectively. We had two findings. One is that with the increase of both l_{rank} and l_{sparse} , the performance of denoising decreases consistently at different noise levels. The other is that PSNR is more sensitive to the variation of l_{sparse} . The observation highlights the potential of active generalization, as Section 4.4 has demonstrated.

Secondly, we further interpreted the relationship between (l_{rank}, l_{sparse}) and image details. As Fig. 9 (c) shows, each image behaves differently in terms of the pair of loss function (l_{rank}, l_{sparse}) . As the level of image rank increases, both l_{rank} and l_{sparse} rise, with l_{sparse} showing a more significant elevation. This suggests that the AG algorithm be more effective in adapting f_{θ_S} via minimizing l_{sparse} . Additionally, l_{sparse} reflects the richness of details and can vary significantly even among images with similar l_{rank} . For instance, samples #1 and #2, whose details are displayed in Fig. 9 (c) and (d), have similar l_{rank} values but differ evidently in texture details. Specifically, sample #1 has a more complex background, leading to a higher value of l_{sparse} , while sample #2 exhibits more self-consistency thus with a lower value of l_{sparse} . Section 6 of Supplementary Material provides more discussion of interpretation.

5 CONCLUSION

In this work, we have proposed a novel framework for developing architecture-modularized and interpretable DNNs for image decomposition and downstream tasks. This framework consists of three steps: modeling image decomposition, formulating inference as two optimization problems, and designing a modularized network informed by the first two steps. We further investigated a generalization error bound, based on which, we proposed a test-time adaptation method for out-of-distribution (OOD) scenarios. Finally, we demonstrated the generalizability and interpretability with two applications, *i.e.*, image denoising and unsupervised anomaly detection.

For future work, firstly models are yet to be developed, capable of integrating different decomposition rules for various applications, such as image super-resolution and inpainting. Secondly, we need to develop new strategies to accommodate more scenarios, by implementing the adaptation either on low-rank module f_{θ_L} or on both modules $(f_{\theta_L}$ and $f_{\theta_S})$ effectively. Last but not least, it is interesting to further explore the advantages of modularization, such as

module reusability across different applications for transfer learning.

ACKNOWLEDGMENTS

This work was funded by the National Natural Science Foundation of China (grant No. 62372115). The authors would like to thank Boming Wang, An Sui, Hangqi Zhou, and Yibo Gao for useful comments and proofreading of the manuscript.

REFERENCES

- [1] D. Ulyanov, A. Vedaldi, and V. Lempitsky, "Deep image prior," in *Proceedings of the IEEE conference on computer vision and pattern recognition*, 2018, pp. 9446–9454.
- [2] Y. Kim, B. Ham, M. N. Do, and K. Sohn, "Structure-texture image decomposition using deep variational priors," *IEEE Transactions on Image Processing*, vol. 28, no. 6, pp. 2692–2704, 2018.
- [3] Y. Gandelsman, A. Shocher, and M. Irani, "Double-dip: unsupervised image decomposition via coupled deep-image-priors," in *Proceedings of the IEEE/CVF Conference on Computer Vision and Pattern Recognition*, 2019, pp. 11 026–11 035.
- [4] A. Buades, B. Coll, and J.-M. Morel, "A review of image denoising algorithms, with a new one," *Multiscale modeling & simulation*, vol. 4, no. 2, pp. 490–530, 2005.
- [5] L. I. Rudin, S. Osher, and E. Fatemi, "Nonlinear total variation based noise removal algorithms," *Physica D: nonlinear phenomena*, vol. 60, no. 1-4, pp. 259–268, 1992.
- [6] E. J. Candès, X. Li, Y. Ma, and J. Wright, "Robust principal component analysis?" *Journal of the ACM*, vol. 58, no. 3, pp. 1–37, May 2011.
- [7] A. Ouahabi, *Signal and image multiresolution analysis*. John Wiley & Sons, 2012.
- [8] S. D. Babacan, M. Luessi, R. Molina, and A. K. Katsaggelos, "Sparse Bayesian Methods for Low-Rank Matrix Estimation," *IEEE Transactions on Signal Processing*, vol. 60, no. 8, pp. 3964–3977, Aug. 2012.
- [9] C. Tomasi and R. Manduchi, "Bilateral filtering for gray and color images," in *Sixth International Conference on Computer Vision*, 1998, pp. 839–846.
- [10] L. Xu, Q. Yan, Y. Xia, and J. Jia, "Structure extraction from texture via relative total variation," *ACM transactions on graphics*, vol. 31, no. 6, pp. 1–10, 2012.
- [11] J. Xu, Y. Guo, W. Shang, and S. You, "Image decomposition combining low-rank and deep image prior," *Multimedia Tools and Applications*, vol. 83, no. 5, pp. 13 887–13 903, 2024.
- [12] M. Zontak and M. Irani, "Internal statistics of a single natural image," in *CVPR 2011*, 2011, pp. 977–984.
- [13] Z. Zhao, S. Xu, C. Zhang, J. Liu, J. Zhang, and P. Li, "Didfuse: deep image decomposition for infrared and visible image fusion," in *Proceedings of the Twenty-Ninth International Joint Conference on Artificial Intelligence*, ser. IJCAI'20, 2021.
- [14] L. Lettry, K. Vanhoey, and L. Van Gool, "Darn: a deep adversarial residual network for intrinsic image decomposition," in *2018 IEEE winter conference on applications of computer vision*. IEEE, 2018, pp. 1359–1367.
- [15] Y. Zhang, P. Tiño, A. Leonardis, and K. Tang, "A survey on neural network interpretability," *IEEE Transactions on Emerging Topics in Computational Intelligence*, vol. 5, no. 5, pp. 726–742, 2021.
- [16] C. Rudin, "Stop explaining black box machine learning models for high stakes decisions and use interpretable models instead," *Nature machine intelligence*, vol. 1, no. 5, pp. 206–215, 2019.
- [17] V. Monga, Y. Li, and Y. C. Eldar, "Algorithm unrolling: Interpretable, efficient deep learning for signal and image processing," *IEEE Signal Processing Magazine*, vol. 38, no. 2, pp. 18–44, 2021.
- [18] R. Liu, S. Cheng, L. Ma, X. Fan, and Z. Luo, "Deep proximal unrolling: Algorithmic framework, convergence analysis and applications," *IEEE Transactions on Image Processing*, vol. 28, no. 10, pp. 5013–5026, 2019.
- [19] S. He, S. Xiong, Z. An, W. Zhang, Y. Huang, and Y. Zhang, "An unsupervised deep unrolling framework for constrained optimization problems in wireless networks," *IEEE Transactions on Wireless Communications*, vol. 21, no. 10, pp. 8552–8564, 2022.

- [20] Q. Zhang, Y. N. Wu, and S.-C. Zhu, "Interpretable convolutional neural networks," in *Proceedings of the IEEE conference on computer vision and pattern recognition*, 2018, pp. 8827–8836.
- [21] S. Gao, H. Zhou, Y. Gao, and X. Zhuang, "Bayeseg: Bayesian modeling for medical image segmentation with interpretable generalizability," *Medical Image Analysis*, vol. 89, p. 102889, 2023.
- [22] D. McAllester, "Simplified pac-bayesian margin bounds," in *Learning Theory and Kernel Machines*, 2003, pp. 203–215.
- [23] S. D. Mbacke, F. Clerc, and P. Germain, "Statistical guarantees for variational autoencoders using pac-bayesian theory," in *Advances in Neural Information Processing Systems*, vol. 36, 2023, pp. 56 903–56 915.
- [24] Z. Zhou, X. Li, J. Wright, E. Candes, and Y. Ma, "Stable principal component pursuit," in *2010 IEEE international symposium on information theory*. IEEE, 2010, pp. 1518–1522.
- [25] E. Candès and B. Recht, "Exact matrix completion via convex optimization," *Commun. ACM*, vol. 55, no. 6, p. 111–119, Jun. 2012.
- [26] C. Peng, Y. Chen, Z. Kang, C. Chen, and Q. Cheng, "Robust principal component analysis: A factorization-based approach with linear complexity," *Information Sciences*, vol. 513, pp. 581–599, 2020.
- [27] Z. Lin, A. Ganesh, J. Wright, L. Wu, M. Chen, and Y. Ma, "Fast convex optimization algorithms for exact recovery of a corrupted low-rank matrix," *Coordinated Science Laboratory Report no. UILU-ENG-09-2214, DC-246*, 2009.
- [28] Z. Lin, M. Chen, and Y. Ma, "The augmented lagrange multiplier method for exact recovery of corrupted low-rank matrices," *arXiv preprint arXiv:1009.5055*, 2010.
- [29] M. Zhou, C. Wang, M. Chen, J. Paisley, D. Dunson, and L. Carin, "Nonparametric bayesian matrix completion," in *2010 IEEE Sensor Array and Multichannel Signal Processing Workshop*. IEEE, 2010, pp. 213–216.
- [30] S. Gao and X. Zhuang, "Rank-One Network: An Effective Framework for Image Restoration," *IEEE Transactions on Pattern Analysis and Machine Intelligence*, vol. 44, no. 6, pp. 3224–3238, Jun. 2022.
- [31] A. Buades, B. Coll, and J.-M. Morel, "A non-local algorithm for image denoising," in *2005 IEEE computer society conference on computer vision and pattern recognition*, vol. 2. Ieee, 2005, pp. 60–65.
- [32] M. Elad and M. Aharon, "Image denoising via sparse and redundant representations over learned dictionaries," *IEEE Transactions on Image processing*, vol. 15, no. 12, pp. 3736–3745, 2006.
- [33] K. Dabov, A. Foi, V. Katkovnik, and K. Egiazarian, "Image denoising by sparse 3-d transform-domain collaborative filtering," *IEEE Transactions on image processing*, vol. 16, no. 8, pp. 2080–2095, 2007.
- [34] X. Hu, R. Ma, Z. Liu, Y. Cai, X. Zhao, Y. Zhang, and H. Wang, "Pseudo 3d auto-correlation network for real image denoising," in *Proceedings of the IEEE/CVF Conference on Computer Vision and Pattern Recognition*, 2021, pp. 16 175–16 184.
- [35] K. Zhang, W. Zuo, Y. Chen, D. Meng, and L. Zhang, "Beyond a gaussian denoiser: Residual learning of deep cnn for image denoising," *IEEE transactions on image processing*, vol. 26, no. 7, pp. 3142–3155, 2017.
- [36] S. Cheng, Y. Wang, H. Huang, D. Liu, H. Fan, and S. Liu, "Nbnnet: Noise basis learning for image denoising with subspace projection," in *Proceedings of the IEEE/CVF conference on computer vision and pattern recognition*, 2021, pp. 4896–4906.
- [37] F. Kokkinos and S. Lefkimmiatis, "Deep image demosaicking using a cascade of convolutional residual denoising networks," in *Proceedings of the European conference on computer vision*, 2018, pp. 303–319.
- [38] J. Kim, J. K. Lee, and K. M. Lee, "Deeply-recursive convolutional network for image super-resolution," in *Proceedings of the IEEE conference on computer vision and pattern recognition*, 2016, pp. 1637–1645.
- [39] M. El Helou and S. Süsstrunk, "Blind universal bayesian image denoising with gaussian noise level learning," *IEEE Transactions on Image Processing*, vol. 29, pp. 4885–4897, 2020.
- [40] A. Abdelhamed, S. Lin, and M. S. Brown, "A high-quality denoising dataset for smartphone cameras," in *IEEE Conference on Computer Vision and Pattern Recognition*, June 2018.
- [41] H. Vu, G. Cheung, and Y. C. Eldar, "Unrolling of deep graph total variation for image denoising," in *ICASSP 2021 - 2021 IEEE International Conference on Acoustics, Speech and Signal Processing*, 2021, pp. 2050–2054.
- [42] J. Liu, Q. Wang, H. Fan, Y. Wang, Y. Tang, and L. Qu, "Residual denoising diffusion models," in *Proceedings of the IEEE/CVF Conference on Computer Vision and Pattern Recognition*, June 2024, pp. 2773–2783.
- [43] H. Chen, J. Gu, Y. Liu, S. A. Magid, C. Dong, Q. Wang, H. Pfister, and L. Zhu, "Masked image training for generalizable deep image denoising," in *Proceedings of the IEEE/CVF Conference on Computer Vision and Pattern Recognition*, 2023, pp. 1692–1703.
- [44] V. Zavrtnik, M. Kristan, and D. Skocaj, "DR \bar{A} EM – A discriminatively trained reconstruction embedding for surface anomaly detection," in *2021 IEEE/CVF International Conference on Computer Vision*, Oct. 2021, pp. 8310–8319.
- [45] M.-I. Georgescu, A. Barbalau, R. T. Ionescu, F. S. Khan, M. Popescu, and M. Shah, "Anomaly detection in video via self-supervised and multi-task learning," in *Proceedings of the IEEE/CVF conference on computer vision and pattern recognition*, 2021, pp. 12 742–12 752.
- [46] Z. Yang, I. Soltani, and E. Darve, "Anomaly detection with domain adaptation," in *Proceedings of the IEEE/CVF Conference on Computer Vision and Pattern Recognition Workshops*, June 2023, pp. 2958–2967.
- [47] Z. You, L. Cui, Y. Shen, K. Yang, X. Lu, Y. Zheng, and X. Le, "A unified model for multi-class anomaly detection," in *Advances in Neural Information Processing Systems*, S. Koyejo, S. Mohamed, A. Agarwal, D. Belgrave, K. Cho, and A. Oh, Eds., vol. 35, 2022, pp. 4571–4584.
- [48] N.-C. Ristea, N. Madan, R. T. Ionescu, K. Nasrollahi, F. S. Khan, T. B. Moeslund, and M. Shah, "Self-supervised predictive convolutional attentive block for anomaly detection," in *Proceedings of the IEEE/CVF Conference on Computer Vision and Pattern Recognition*, June 2022, pp. 13 576–13 586.
- [49] S. Akçay, A. Atapour-Abarghouei, and T. P. Breckon, "Skip-ganomaly: Skip connected and adversarially trained encoder-decoder anomaly detection," in *2019 International Joint Conference on Neural Networks*. IEEE, 2019, pp. 1–8.
- [50] M. Hasan, J. Choi, J. Neumann, A. K. Roy-Chowdhury, and L. S. Davis, "Learning temporal regularity in video sequences," in *Proceedings of the IEEE conference on computer vision and pattern recognition*, 2016, pp. 733–742.
- [51] D. Dehaene and P. Eline, "Anomaly localization by modeling perceptual features," *arXiv preprint arXiv:2008.05369*, 2020.
- [52] Z. Liu, Y. Nie, C. Long, Q. Zhang, and G. Li, "A hybrid video anomaly detection framework via memory-augmented flow reconstruction and flow-guided frame prediction," in *Proceedings of the IEEE/CVF International Conference on Computer Vision*, 2021, pp. 13 588–13 597.
- [53] J. Yu, Y. Zheng, X. Wang, W. Li, Y. Wu, R. Zhao, and L. Wu, "Fastflow: Unsupervised anomaly detection and localization via 2d normalizing flows," *arXiv preprint arXiv:2111.07677*, 2021.
- [54] T. DeVries and G. W. Taylor, "Improved regularization of convolutional neural networks with cutout," *arXiv preprint arXiv:1708.04552*, 2017.
- [55] C.-L. Li, K. Sohn, J. Yoon, and T. Pfister, "Cutpaste: Self-supervised learning for anomaly detection and localization," in *Proceedings of the IEEE/CVF conference on computer vision and pattern recognition*, 2021, pp. 9664–9674.
- [56] Z. Li, N. Li, K. Jiang, Z. Ma, X. Wei, X. Hong, and Y. Gong, "Superpixel masking and inpainting for self-supervised anomaly detection," in *Bmvc*, 2020.
- [57] X. Yan, H. Zhang, X. Xu, X. Hu, and P.-A. Heng, "Learning semantic context from normal samples for unsupervised anomaly detection," in *Proceedings of the AAAI Conference on Artificial Intelligence*, vol. 35, no. 4, 2021, pp. 3110–3118.
- [58] P. Bergmann, M. Fauser, D. Sattlegger, and C. Steger, "Uninformed students: Student-teacher anomaly detection with discriminative latent embeddings," in *Proceedings of the IEEE/CVF conference on computer vision and pattern recognition*, 2020, pp. 4183–4192.
- [59] G. Pang, C. Shen, L. Cao, and A. V. D. Hengel, "Deep learning for anomaly detection: A review," *ACM Comput. Surv.*, vol. 54, no. 2, Mar. 2021.
- [60] F. Keller, E. Muller, and K. Bohm, "Hics: High contrast subspaces for density-based outlier ranking," in *2012 IEEE 28th international conference on data engineering*. IEEE, 2012, pp. 1037–1048.
- [61] D. M. Blei, A. Kucukelbir, and J. D. McAuliffe, "Variational inference: A review for statisticians," *Journal of the American statistical Association*, vol. 112, no. 518, pp. 859–877, 2017.
- [62] C. Zhang, J. Bütepage, H. Kjellström, and S. Mandt, "Advances in variational inference," *IEEE transactions on pattern analysis and machine intelligence*, vol. 41, no. 8, pp. 2008–2026, 2018.
- [63] D. H. Wolpert and W. G. Macready, "No free lunch theorems for optimization," *IEEE transactions on evolutionary computation*, vol. 1, no. 1, pp. 67–82, 1997.

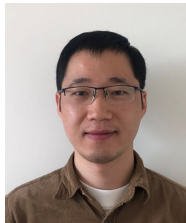
- [64] J. Baxter, "A model of inductive bias learning," *Journal of artificial intelligence research*, vol. 12, pp. 149–198, 2000.
- [65] A. Goyal and Y. Bengio, "Inductive biases for deep learning of higher-level cognition," *Proceedings of the Royal Society A*, vol. 478, no. 2266, p. 20210068, 2022.
- [66] S. Gao and X. Zhuang, "Bayesian image super-resolution with deep modeling of image statistics," *IEEE Transactions on Pattern Analysis and Machine Intelligence*, vol. 45, no. 2, pp. 1405–1423, 2023.
- [67] C. Doersch, "Tutorial on variational autoencoders," *arXiv preprint arXiv:1606.05908*, 2016.
- [68] K. He, X. Zhang, S. Ren, and J. Sun, "Deep residual learning for image recognition," in *Proceedings of the IEEE conference on computer vision and pattern recognition*, 2016, pp. 770–778.
- [69] P. Germain, F. Bach, A. Lacoste, and S. Lacoste-Julien, "Pac-bayesian theory meets bayesian inference," in *Advances in Neural Information Processing Systems*, D. Lee, M. Sugiyama, U. Luxburg, I. Guyon, and R. Garnett, Eds., vol. 29, 2016.
- [70] M. Fazlyab, A. Robey, H. Hassani, M. Morari, and G. Pappas, "Efficient and accurate estimation of lipschitz constants for deep neural networks," in *Advances in Neural Information Processing Systems*, vol. 32, 2019.
- [71] G. Blanchard, M. Hoffmann, and M. Reiß, "Optimal adaptation for early stopping in statistical inverse problems," *SIAM/ASA Journal on Uncertainty Quantification*, vol. 6, no. 3, pp. 1043–1075, 2018.
- [72] E. Agustsson and R. Timofte, "Ntire 2017 challenge on single image super-resolution: Dataset and study," in *The IEEE Conference on Computer Vision and Pattern Recognition Workshops*, July 2017.
- [73] S. Roth and M. J. Black, "Fields of experts: A framework for learning image priors," in *2005 IEEE Computer Society Conference on Computer Vision and Pattern Recognition*, vol. 2. IEEE, 2005, pp. 860–867.
- [74] R. Franzen, "Kodak lossless true color image suite," *source: http://r0k.us/graphics/kodak*, vol. 4, no. 2, p. 9, 1999.
- [75] L. Zhang, X. Wu, A. Buades, and X. Li, "Color demosaicking by local directional interpolation and nonlocal adaptive thresholding," *Journal of Electronic imaging*, vol. 20, no. 2, pp. 023 016–023 016, 2011.
- [76] J. Xu, H. Li, Z. Liang, D. Zhang, and L. Zhang, "Real-world noisy image denoising: A new benchmark," *arXiv preprint arXiv:1804.02603*, 2018.
- [77] P. Bergmann, M. Fauser, D. Sattlegger, and C. Steger, "Mvtec ad—a comprehensive real-world dataset for unsupervised anomaly detection," in *Proceedings of the IEEE/CVF conference on computer vision and pattern recognition*, 2019, pp. 9592–9600.
- [78] K. Severstal, "Steel defect detection," *Can You Detect and Classify Defects in Steel*, 2019.
- [79] T. Cao, C.-W. Huang, D. Y.-T. Hui, and J. P. Cohen, "A benchmark of medical out of distribution detection," *arXiv preprint arXiv:2007.04250*, 2020.
- [80] J. Davis and M. Goadrich, "The relationship between precision-recall and roc curves," in *Proceedings of the 23rd international conference on Machine learning*, 2006, pp. 233–240.
- [81] D. P. Kingma and J. Ba, "Adam: A method for stochastic optimization," *arXiv preprint arXiv:1412.6980*, 2014.
- [82] K. Dabov, A. Foi, V. Katkovnik, and K. Egiazarian, "Image denoising by sparse 3-d transform-domain collaborative filtering," *IEEE Transactions on image processing*, vol. 16, no. 8, pp. 2080–2095, 2007.
- [83] K. Zhang, W. Zuo, Y. Chen, D. Meng, and L. Zhang, "Beyond a gaussian denoiser: Residual learning of deep cnn for image denoising," *IEEE transactions on image processing*, vol. 26, no. 7, pp. 3142–3155, 2017.
- [84] K. Zhang, W. Zuo, and L. Zhang, "Ffdnet: Toward a fast and flexible solution for cnn-based image denoising," *IEEE Transactions on Image Processing*, vol. 27, no. 9, pp. 4608–4622, 2018.
- [85] S. Gao and X. Zhuang, "Rank-one network: An effective framework for image restoration," *IEEE Transactions on Pattern Analysis and Machine Intelligence*, vol. 44, no. 6, pp. 3224–3238, 2022.
- [86] Z. Yue, H. Yong, Q. Zhao, L. Zhang, D. Meng, and K.-Y. K. Wong, "Deep variational network toward blind image restoration," *IEEE Transactions on Pattern Analysis and Machine Intelligence*, 2024.
- [87] G. Wang, S. Han, E. Ding, and D. Huang, "Student-teacher feature pyramid matching for unsupervised anomaly detection," *arXiv preprint arXiv:2103.04257*, 2021.



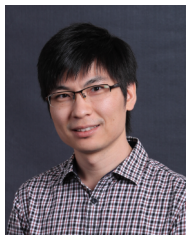
Sihan Wang is doing a Ph.D. at the School of Data Science, Fudan University, Shanghai, China, with Prof. Xiahai Zhuang. She received her Bachelor's degree from Fudan University in 2021. Her current research interests focus on model interpretability, generalizability, and modularity for computer vision, with applications in tasks such as image restoration and segmentation.



Shanggqi Gao is a Research Associate at the University of Cambridge. Before that, he was a Research Assistant at the University of Oxford. He got his Ph.D. in School of Data Science, Fudan University, in 2022. Before that he had both M.Sc and B.S. degrees in Mathematics and Statistics. His current research interests include computational imaging, medical image analysis and explainable AI. His work won the Elsevier-MedIA 1st Prize and Medical image Analysis MICCAI Best Paper Award 2023.



Fuping Wu is a Research Associate at the University of Oxford. He graduated from Huazhong University of Science and Technology in 2012. He received an MSc degree from Wuhan University in 2016, and a PhD degree from Fudan University in 2021. His current research interests include medical image analysis and computer vision.



Xiahai Zhuang is a professor at School of Data Science, Fudan University. He graduated from the Department of Computer Science, Tianjin University, received a Master's degree from Shanghai Jiao Tong University, and a Doctorate degree from University College London. His research interests include interpretable AI, medical image analysis and computer vision. His work won the Elsevier-MedIA 1st Prize and Medical image Analysis MICCAI Best Paper Award 2023.